PPPL-3138 - Preprint: August 1995, UC-420, 421, 427

Conceptual Study of Electron Ripple Injection for Tokamak Transport Control

W. Choe, M. Ono, and C.S. Chang

RECEIVED
MAR 11 1996
OSTI

COPIES

-ps

Conceptual Study of Electron Ripple Injection for Tokamak Transport Control

W. Choe, M. Ono, and C.S. Chang*
Plasma Physics Laboratory, Princeton University
Princeton, NJ 08543
*Courant Institute of Mathematical Sciences
New York University, 251 Mercer Street, New York
New York 10012

A non-intrusive method for inducing radial electric field based on electron ripple injection is under development by the Princeton CDX-U group. The radial electric field is known to play an important role in the L-H and H-VH mode transition according to the recent theoretical and experimental research. It is therefore important to develop a non-intrusive tool to control the radial electric field profile in tokamak plasmas. The present technique utilizes externally-applied local magnetic ripple fields to trap electrons at the edge, allowing them to penetrate towards the plasma center via ∇B and curvature drifts, causing the flux surfaces to charge up negatively. Electron cyclotron resonance heating is utilized to increase the trapped population and the electron drift velocity by raising the perpendicular energy of trapped electrons. In order to quantify the effects of cyclotron resonance heating on electrons, the temperature anisotropy of resonant electrons in a tokamak plasma is calculated. For the calculation of anisotropic temperatures, energy moments of the bounce-averaged Fokker-Planck equation with a bi-Maxwellian distribution function for heated electrons are solved, assuming a moderate wave power and a constant quasilinear diffusion coefficient. Simulation using a guiding-center orbit model have been performed to understand the behavior of suprathermal electrons in the presence of ripple fields. Examples for CDX-U and ITER parameters are given.

1. INTRODUCTION

Since the discovery of the H-mode in ASDEX [1] over a decade ago, many devices have confirmed and further extended this improved confinement regime by various methods [2–26]. One of the most important characteristics of this mode is that the global energy confinement time is two or three times longer than that in conventional L-mode plasmas. The global particle confinement time in H-mode is also significantly increased. The onset of this mode can be identified by the formation of a transport barrier at the plasma edge where density and temperature gradients steepen after the transition, suggesting better particle and energy confinement. When there is a barrier formation, a radial electric field is also known to develop at the plasma edge [26–30] and this electric field accompanies a plasma rotation which is believed to play a crucial role in the plasma transition to better confinement regimes. In recent years, the confinement improvement zone is observed to be extended inward toward the plasma core when the plasma makes transition from H-mode to VH mode. The energy confinement in VH-mode is observed to be about twice of that of the ELM-free H-modes of both DIII-D [31–36] and JET [37].

Based on these findings, the first question we can ask ourselves is what exactly triggers those improved modes. To date, the prevailing hypothesis for the L-H and H-VH mode transition is the stabilization of turbulence due to sheared $\mathbf{E} \times \mathbf{B}$ flow [38, 39] and the reasons why $\mathbf{E} \times \mathbf{B}$ shear is considered as a the fundamental quantity are addressed in Ref. [34]. The present so-called H-mode scaling for future devices suggests that a very high power threshold ($> 100\,MW$) is required to induce H-mode discharges on ITER [40]. Then, it would be quite natural to ask next whether it is possible to generate radial electric fields by external means and thereby to develop more efficient ways to achieve improved confinement in large scale future devices. Some efforts to accomplish this goal have already been attempted. CCT [2] and other experiments [3, 4] produced an H-mode plasma by an externally-injected radial current from a biased electrode inserted into the plasma. In order to apply the same principle to high density and temperature plasmas, however, one must consider other methods which are compatible and extendable to such plasmas since material electrodes placed in those plasmas would be rapidly destroyed. This is the motivation for developing the electron ripple injection (ERI) method [41, 42], i.e., to induce radial electric fields in a non-intrusive way. This technique has the advantages that the physics is relatively simple, it is non-intrusive, easily controllable, and therefore applicable to larger size fusion devices.

The electron ripple injection concept is designed to produce a radial electric field at the plasma edge by injecting electrons into the plasma interior. Electrons having much larger perpendicular energy than parallel energy due to electron cyclotron resonance heating will be trapped in a spatially localized magnetic field ripple region provided by local poloidal field bending magnets. These trapped electrons will move toward the plasma center by ∇B and curvature drifts. The ripple-trapped electrons will eventually be detrapped due to collisions between the particles, resulting in charging the plasma negatively where detrapping occurs.

Cyclotron resonance heating is known to increase preferentially the perpendicular energy of resonant particles so that the distribution function of the heated particles is no longer isotropic. In this paper, we calculate the anisotropic temperatures of electron cyclotron resonance heated particles with a bi-Maxwellian model of warm electron distribution. For the sake of simplicity, we assume small inverse aspect ratio and circular magnetic flux surfaces; and neglect the relativistic and Doppler shift effects in the wave-particle interaction.

In the presence of local ripple fields, the magnetic field structure becomes rather complicated. It would therefore be instructive to simulate numerically the motion of an energetic electron having a predominantly perpendicular energy in order to test the feasibility of the electron injection scenario. A Monte-Carlo electron guiding-center orbit code has been developed for this purpose.

In Section 2, a more detailed discussion of the electron ripple injection concept is presented, and the temperature anisotropy is calculated in Section 3. Results from electron guiding-center orbit calculations in the presence of ripple fields are shown in Section 4. Finally, a summary is given in Section 5.

2. CONCEPTUAL DESIGN OF RIPPLE INJECTOR

The electron ripple injection concept is designed to produce a radial electric field at the plasma edge by injecting electrons into the plasma interior. The electrons which have much larger perpendicular energy than parallel energy by electron cyclotron resonance heating will be trapped in a small local magnetic field ripple region provided by local poloidal field bending magnets (see *Fig.* 1 and *Fig.* 2). By placing the ripple region appropriately, these trapped electrons will move toward the plasma center by ∇B and curvature drifts. Since the direction of these drifts depends upon the toroidal field direction, the electron injector should be placed either at the top or bottom of a torus in order for the drift direction to point toward the plasma center. The ripple-trapped electrons will eventually be detrapped due to collisions between the particles and due to the decrease of field ripple strength away from the ripple source. The ripple strength is defined as,

$$\delta(\%) = \frac{B_{max} - B_{min}}{B_{max} + B_{min}} \times 100, \tag{1}$$

where B_{max} and B_{min} are maximum and minimum fields in the ripple region, and if δ is 5%, then the trapping condition would be

$$\frac{v_\perp}{v_\parallel} \geq \left(\frac{2\delta}{1-\delta}\right)^{-1/2} \simeq 3.$$

Therefore, it is important to have electrons which have predominantly perpendicular energy.

In the design of ripple coils, a few requirements should be satisfied. First, as discussed earlier, the coils should be positioned appropriately to provide drift of the ripple-trapped electrons toward the plasma center before detrapping takes place. Second, the ripple strength must be high enough in the ripple region, but the radial variation of the ripple strength must be sufficiently rapid in order for drifting electrons to become detrapped after drifting a desired radial distance. Third, the ripple strength should be kept minimum to prevent serious plasma perturbation. According to the experimental results in DIII-D [26], the thickness of the electric field layer during H-mode transition appears to be $1 - 3\,cm$ inside the last closed flux surface. This suggests that the radial penetration distance of injected electrons which is determined by ripple strength and electron energy needs to be at least of this order. Considering all these requirements, δ would be typically a few percent for electron ripple injection experiments.

Several configurations of ripple coils were studied for ripple-assisted neutral beam injection [43]. For our purposes, we consider a configuration shown in *Fig.* 1 and *Fig.* 2 where a pair of rectangular-shaped ripple coils are vertically aligned toroidally in order to provide a desired amount of field ripple. In order to visualize the generation of local magnetic well out of these coils, the magnetic field line equations with the Biot-Savart law were solved to trace each field line in cylindrical coordinates (R, ϕ, Z) where R, ϕ, Z are major radial, toroidal, and vertical coordinates, respectively:

$$\frac{dR}{B_R} = \frac{R\,d\phi}{B_\phi} = \frac{dZ}{B_Z} = \frac{d\ell}{B}, \tag{2}$$

where $d\ell = [(dR)^2 + (d\phi)^2 + (dZ)^2]^{1/2}$ is the arc length. In the present work, the radial direction always means the direction of increasing major radius unless otherwise specified. The ripple field is calculated by modeling the ripple coils with filamentary currents. For the calculation, ripple coils are assumed to be located at $R = 35\,cm$, $Z = 42\,cm$ on CDX-U device. *Figure* 3 depicts several different magnetic field lines with $B_0 = 1\,kG$, $R_0 = 35\,cm$, and the ripple coil current $I_{rip} = 10\,kA\cdot turn$. The figure shows radially-outward field line bending and the generation of a local magnetic well around ripple coils. With this value of ripple coil currents, a ripple strength of 5.8 % can be obtained. The poloidal field is not included for the calculation and the addition of poloidal field simply makes field lines oblique. *Figure* 4 shows a different view of the total field strength. This figure clearly shows the generation of toroidally localized magnetic well that arises from the $1/R$-dependent toroidal field. *Figure* 5 is a contour plot of ripple strength and the localization of the field ripple is seen around the ripple coils. We should note that this localized ripple field is inherently different from the ripple fields of toroidal magnets. Here, the effective 'ripple' is produced without introducing the regular toroidal field ripple structures.

To increase the collisionless trapped electron population with energies of a few keV in the ripple region and to provide larger drifts, electrons must have large perpendicular speed compared to parallel speed. For this purpose, electron cyclotron resonance heating is appropriate. Preferential heating in perpendicular direction means the distribution function of resonant electrons is no longer isotropic. In the next section, a quantitative calculation of temperature anisotropy driven by electron cyclotron resonance heating is presented using a bi-Maxwellian model.

3. KINETIC CALCULATION OF TEMPERATURE ANISOTROPY

We assume that the background particles satisfy the Maxwellian distribution, and that the density of warm particles is small compared to that of background particles. We neglect Coulomb self-collisions between the warm particles when compared to the collisions of the warm particles with the background particles. Plasma particles are divided into four different species: background cold electron (e) and ion (i) species, cold impurity species (I), and warm electron species (w) heated by the waves.

We write a model Fokker-Planck equation for the warm electrons in the form

$$\frac{\partial f}{\partial t} = \mathcal{C}(f) + \mathcal{Q}(f) + \mathcal{L}(f) + \mathcal{S}, \tag{3}$$

where $\mathcal{C}$ is the Coulomb collision operator, $\mathcal{Q}$ is the wave heating operator, $\mathcal{L}(f)$ represents the rapid loss of particles due to drift of ripple-trapped electrons, and $\mathcal{S}$ is the source of the warm electrons. If we use $\mathbf{v}_L$ to denote the vertical drift velocity

$$\mathbf{v}_L = \frac{m_e(v_\perp^2 + 2v_\parallel^2)}{2e} \frac{\nabla B \times \mathbf{B}}{B^3}, \tag{4}$$

then the ripple loss operator can be modeled as

$$\mathcal{L}(f) = -\chi \nabla \cdot (\mathbf{v_L} f),$$

where χ is the fraction of the ripple-trapped electrons. If we define a characteristic scale length L,

$$L^{-1} \equiv \frac{\nabla \cdot (\mathbf{v_L} f)}{v_L f},$$

we can write a characteristic drift loss rate due to ripple-trapping as

$$\nu_L = \frac{T_e}{e} \frac{1}{RB} \frac{1}{L}. \tag{5}$$

Then, the ripple loss operator can be expressed in the form

$$\mathcal{L}(f) = -\chi \frac{\nu_L}{v_e^2} (v_\perp^2 + 2v_\parallel^2) f. \tag{6}$$

The warm electrons are lost by the ripple-trapping effect, but they are continuously replenished from the cold background electrons by wave heating. We model the warm electron source term as

$$\mathcal{S} = \eta f_M, \tag{7}$$

where f_M is the Maxwellian distribution function for the background electrons and η is a source coefficient. In steady-state, the loss and source will have to balance.

For an efficient ripple-trapping, the electron collision frequency needs to be low. By requiring the effective Coulomb scattering rate ν_c/δ from the ripple well to be smaller than ν_L, we have

$$\frac{\nu_c R}{v_e} < \delta \frac{\rho_e}{L},$$

as shown in Ref. [44] where ρ_e is the electron gyroradius. By rearranging the above equation, the critical warm electron energy above which the collisionless radial loss model holds can be obtained as

$$\begin{aligned} T_w &> T_{crit}\,, \\ T_{crit}(eV) &= \left[\frac{3.5\times 10^{11}}{\delta(\%)}\, L(m)\, R(m)\, n_e(10^{20}\, m^{-3})\, B(T)\right]^{2/5} . \end{aligned} \tag{8}$$

With typical CDX-U parameters ($n_e = 2\times 10^{18}\, m^{-3}$, $R = 0.35\, m$, $B = 0.1\, T$, and $\delta = 5\,\%$), the critical energy is $360\, eV$ if we take $L = 0.05\, m$.

Since the electron cyclotron heating discriminates perpendicular from parallel direction, we need to consider the perpendicular and parallel energy separately. Energy conservation in steady-state then gives us two equations

$$\left\langle \int d^3v\, v_\perp^2 \left[\mathcal{C} - \chi\, \frac{\nu_L}{v_e^2}\left(v_\perp^2 + 2v_\parallel^2\right) f + \eta\, f_M + \mathcal{Q}\right](f)\right\rangle = 0, \tag{9}$$

$$\left\langle \int d^3v\, v_\parallel^2 \left[\mathcal{C} - \chi\, \frac{\nu_L}{v_e^2}\left(v_\perp^2 + 2v_\parallel^2\right) f + \eta\, f_M \right](f)\right\rangle = 0. \tag{10}$$

The parallel energy moment equation does not have a wave heating term. This is because we assume that the parallel wave number in the quasilinear operator is small so that the particles are heated only in the perpendicular direction [45].

The procedure to obtain solutions from *Eqs.* (9) and (10) has been shown in Ref. [46] when there is no ripple field, and the same procedure will also be adopted here. In the present paper, the (v, λ) coordinate system is chosen for particle velocity in which λ is a constant of motion and defined as

$$\lambda \equiv \frac{B_m}{B}\frac{v_\perp^2}{v^2},$$

where B_m is the magnetic field at the minimum Mod-B point. The Jacobian in these velocity coordinates is calculated to be

$$\int d^3v = \sum_\sigma \int \frac{\pi v^3}{|v_\parallel|}\frac{B}{B_m} d\lambda\, dv,$$

where $\sigma = v_\parallel/|v_\parallel|$.

In flux coordinates (ψ, θ, ζ), where ψ, θ, ζ are radial, poloidal, and toroidal coordinates, respectively, it can be shown [47] that the flux surface average over a velocity integration of a physical quantity g can be reduced to a velocity integral if the bounce-averaged value of g is known:

$$\left\langle \int d^3v\, g\right\rangle = \frac{\pi}{B_m \int \mathcal{J} d\theta} \sum_\sigma \int d\lambda\, dv\, v^3\, \tau_b\, \{g\}, \tag{11}$$

where $\mathcal{J}$ is the Jacobian for the flux coordinates. The bounce time is defined as

$$\tau_b = \int \frac{\mathcal{J} B \, d\theta}{|v_{\parallel}|}. \tag{12}$$

The integration range of θ is taken between $-\pi \leq \theta \leq \pi$ for passing particles and $-\theta_t \leq \theta \leq \theta_t$ for trapped particles where θ_t is the poloidal angle of the banana tips. In addition, since the integrand for a bounce time, τ_b, is proportional to $1/v_{\parallel}$, $\hat{\tau}_b (\equiv v \, \tau_b)$ is independent of v, but dependent on λ.

Using *Eq.* (11), *Eqs.* (9) and (10) can be expressed as

$$\int_0^1 d\lambda \int_0^{\infty} dv \, v^2 \, \hat{\tau}_b \left\{ v_{\perp}^2 \mathcal{C} \right\} (f) \; - (Loss)_{\perp} + (Source)_{\perp} + (Heating)_{\perp} = 0, \tag{13}$$

$$\int_0^1 d\lambda \int_0^{\infty} dv \, v^2 \, \hat{\tau}_b \left\{ v_{\parallel}^2 \mathcal{C} \right\} (f) \; - (Loss)_{\parallel} + (Source)_{\parallel} = 0, \tag{14}$$

where

$$(Heating)_{\perp} = \left(\frac{\pi}{B_m \int \mathcal{J} d\theta} \right)^{-1} \left\langle \int d^3 v \, v_{\perp}^2 \, \mathcal{Q}(f) \right\rangle, \tag{15}$$

$$(Loss)_{\parallel}^{\perp} = \frac{\nu_L}{v_e^2} \, \chi \int_0^1 d\lambda \int_0^{\infty} dv \, v^2 \, \hat{\tau}_b \begin{bmatrix} \left\{ v_{\perp}^2 \left(v^2 + v_{\parallel}^2 \right) \right\} f \\ \left\{ v_{\parallel}^2 \left(v^2 + v_{\parallel}^2 \right) \right\} f \end{bmatrix}, \tag{16}$$

$$(Source)_{\parallel}^{\perp} = \eta \int_0^1 d\lambda \, \hat{\tau}_b \begin{bmatrix} \left\{ v_{\perp}^2 \right\} \\ \left\{ v_{\parallel}^2 \right\} \end{bmatrix} \int_0^{\infty} dv \, v^2 f_M. \tag{17}$$

The upper (lower) part in the loss and the source terms indicates the perpendicular (parallel) term. The above two equations (13) and (14) show the appropriate path of energy flow from the input wave to the resonant particles. The heating term, *Eq.* (15) represents the energy input from the wave and it is positive definite. The Coulomb scattering part represents transfer of energy to the background species by energy scattering and redistribution of it within the warm species by pitch angle scattering.

To estimate the anisotropic temperatures from *Eqs.* (13) and (14), a bi-Maxwellian distribution function (which is constant along field lines) is used for the warm particles:

$$f = f_N \left(\alpha_{\perp}^2, \alpha_{\parallel}^2 \right) \cdot e^{-v^2 \left(\frac{\lambda}{\alpha_{\perp}^2} + \frac{1-\lambda}{\alpha_{\parallel}^2} \right)} = f_N \, e^{-b\,(c-\lambda)\, \frac{v^2}{v_e^2}}, \tag{18}$$

where

$$b = \frac{s-1}{\alpha_{\perp}^2 / v_e^2}, \qquad c = \frac{s}{s-1}, \qquad s = \frac{\alpha_{\perp}^2}{\alpha_{\parallel}^2} = \frac{T_{\perp}}{T_{\parallel}}.$$

Here $kT_\perp(= m_e\alpha_\perp^2/2)$ and $kT_\parallel(= m_e\alpha_\parallel^2/2)$ are effective temperatures perpendicular and parallel to magnetic field lines, v_e is background electron thermal speed, and f_N is the normalization factor. We now evaluate each term in *Eqs*. (13) and (14) separately.

3.1. *Coulomb collision term*

The Coulomb collision operator for warm electrons is a combination of pitch angle operator (C_ξ) and energy scattering operator (C_ϵ):

$$C(f) = C_\xi(f) + C_\epsilon(f),$$

where

$$\begin{aligned} C_\xi(f) &= \frac{1}{2}\nu_\xi \frac{\partial}{\partial\xi}(1-\xi^2)\frac{\partial}{\partial\xi}f, && (19)\\ C_\epsilon(f) &= \frac{1}{v^2}\frac{\partial}{\partial v}v^2\,\nu_\epsilon\left(vf + \frac{v_e^2}{2}\frac{\partial f}{\partial v}\right), && (20)\\ \nu_\xi &\approx \nu_0\left(\frac{v_e}{v}\right)^3\left(Z_{eff} + \phi_1\left(\frac{v}{v_e}\right)\right), \\ \nu_\epsilon &\approx \nu_0\left(\frac{v_e}{v}\right)^3\phi_2\left(\frac{v}{v_e}\right), \\ \nu_0 &= \frac{\sqrt{2}\pi\, n_e\, e^4\, ln\Lambda}{\sqrt{m_e}\,(kT_e)^{3/2}}. && (21) \end{aligned}$$

The first term in ν_ξ (which contains Z_{eff}) is from the scattering of warm electrons on background ions, and the second term is from scattering on background electrons. For the energy scattering operator, the contribution from the background electrons is dominant over that from the cold ions by the ion-electron mass ratio, thus, the ion term can be ignored in the warm electron energy scattering operator. The functions in collison frequencies are expressed as

$$\begin{aligned} \phi_1(u) &= \left(1 - \frac{1}{2u^2}\right)Erf(u) + \frac{e^{-u^2}}{\sqrt{\pi}\,u}, \\ \phi_2(u) &= Erf(u) - \frac{2}{\sqrt{\pi}}ue^{-u^2}. \end{aligned}$$

The bounce-averaged Coulomb collision terms in *Eq*. (13) and *Eq*. (14) can be written as

$$\{v_\perp^2 C\}(f) = \{v_\perp^2 C_\xi\}(f) + \{v_\perp^2 C_\epsilon\}(f),$$
$$\left\{v_\parallel^2 C\right\}(f) = \left\{v_\parallel^2 C_\xi\right\}(f) + \left\{v_\parallel^2 C_\epsilon\right\}(f).$$

The energy scattering operator $C_\epsilon(f)$ can be taken out of the bounce integral since it is a function of v only and, thus, constant of motion,

$$\left\{v_\perp^2 C_\epsilon\right\}(f) = \left\{v_\perp^2\right\} C_\epsilon(f), \tag{22}$$

$$\left\{v_\parallel^2 C_\epsilon\right\}(f) = \left\{v_\parallel^2\right\} C_\epsilon(f). \tag{23}$$

The pitch angle scattering operator, *Eq.* (19), can be expressed in terms of the new coordinates (v, λ) as

$$C_\xi = 2\,\nu_\xi \frac{B_m}{B}\,\xi\,\frac{\partial}{\partial\lambda}\,\lambda\,\xi\,\frac{\partial}{\partial\lambda},$$

where $\xi = \sigma\sqrt{1 - \dfrac{B}{B_m}\lambda}$ and the 90° Coulomb collision frequency ν_ξ is a function of v only. Using the relationships,

$$\frac{v_\parallel^2}{v^2} = \xi^2 = 1 - \frac{B}{B_m}\lambda, \qquad \text{and} \qquad \frac{v_\perp^2}{v^2} = 1 - \xi^2 = \frac{B}{B_m}\lambda,$$

we obtain the bounce averages of $v_\perp^2\, C_\xi(f)$ and $v_\parallel^2\, C_\xi(f)$ as

$$\hat{\tau}_b\left\{v_\perp^2\, C_\xi(f)\right\} = 2\,\nu_\xi\, v^2\,\lambda\left[-\hat{\tau}_b\,\frac{1}{2}\,\frac{\partial f}{\partial\lambda} + \frac{\hat{\tau}_b}{v^2}\left\{v_\parallel^2\right\}\left(\frac{\partial}{\partial\lambda}\,\lambda\,\frac{\partial f}{\partial\lambda} + \frac{1}{2}\,\frac{\partial f}{\partial\lambda}\right)\right], \tag{24}$$

$$\hat{\tau}_b\left\{v_\parallel^2\, C_\xi(f)\right\} = 2\,\nu_\xi\, v^2\left[\frac{\hat{\tau}_b}{v^2}\left\{\frac{B_m}{B}v_\parallel^2\right\}\frac{\partial}{\partial\lambda}\,\lambda\,\frac{\partial f}{\partial\lambda} - \frac{\hat{\tau}_b}{v^2}\left\{v_\parallel^2\right\}\lambda\left(\frac{\partial}{\partial\lambda}\,\lambda\,\frac{\partial f}{\partial\lambda} + \frac{1}{2}\,\frac{\partial f}{\partial\lambda}\right)\right]. \tag{25}$$

The complete form of $\hat{\tau}_b$, $\dfrac{\hat{\tau}_b}{v^2}\left\{v_\parallel^2\right\}$, $\dfrac{\hat{\tau}_b}{v^2}\left\{v_\perp^2\right\}$, and $\dfrac{\hat{\tau}_b}{v^2}\left\{\dfrac{B_m}{B}v_\parallel^2\right\}$ are found in Ref. [46]. The detailed calculation of τ_b and $\dfrac{\hat{\tau}_b}{v^2}\left\{v_\perp^2\right\}$ indicates that there exists a singularity at the trapped-passing boundary. Instead of using the complete forms, we replace those bounced-averaged quantities with well behaved ones which are obtained by smoothing the complete forms based on polynomials of λ to avoid numerical problems associated with this singularity:

$$\begin{aligned}
\hat{\tau}_b &\approx V_{tt}(\lambda),\\
\frac{\hat{\tau}_b}{v^2}\left\{v_\parallel^2\right\} &\approx V_{tl}(\lambda),\\
\frac{\hat{\tau}_b}{v^2}\left\{v_\perp^2\right\} &\approx V_{tp}(\lambda),\\
\frac{\hat{\tau}_b}{v^2}\left\{\frac{B_m}{B}v_\parallel^2\right\} &\approx V_{tb}(\lambda),
\end{aligned}$$

where V_{tt}, V_{tl}, V_{tp}, and V_{tb} are shown in Ref. [46]. With the help of these smoothed functions, *Eqs.* (22) - (25) become

$$\hat{r}_b \left\{ v_\perp^2 \, C_\xi(f) \right\} = \frac{2\,\nu_0\, v_e^2}{u} \left(Z_{\mathit{eff}} + \phi_1(u) \right) \lambda \left[-V_{tt}(\lambda) \frac{1}{2} \frac{\partial f}{\partial \lambda} + V_{tl}(\lambda) \left(\frac{\partial}{\partial \lambda} \lambda \frac{\partial f}{\partial \lambda} + \frac{1}{2} \frac{\partial f}{\partial \lambda} \right) \right], \tag{26}$$

$$\hat{r}_b \left\{ v_\parallel^2 \, C_\xi(f) \right\} = \frac{2\,\nu_0\, v_e^2}{u} \left(Z_{\mathit{eff}} + \phi_1(u) \right) \left[V_{tb}(\lambda) \frac{\partial}{\partial \lambda} \lambda \frac{\partial f}{\partial \lambda} - V_{tl}(\lambda)\, \lambda \left(\frac{\partial}{\partial \lambda} \lambda \frac{\partial f}{\partial \lambda} + \frac{1}{2} \frac{\partial f}{\partial \lambda} \right) \right], \tag{27}$$

$$\hat{r}_b \left\{ v_\perp^2 \, C_\epsilon(f) \right\} = \nu_0\, v_e^2\, V_{tp}(\lambda) \frac{\partial}{\partial u} \phi_2(u) \left(f + \frac{1}{2u} \frac{\partial f}{\partial u} \right), \tag{28}$$

$$\hat{r}_b \left\{ v_\parallel^2 \, C_\epsilon(f) \right\} = \nu_0\, v_e^2\, V_{tl}(\lambda) \frac{\partial}{\partial u} \phi_2(u) \left(f + \frac{1}{2u} \frac{\partial f}{\partial u} \right), \tag{29}$$

where $u = v/v_e$.

3.2. Wave heating term

For the quasilinear operator $\mathcal{Q}(f)$, we use

$$\mathcal{Q}(f) = \frac{1}{v_\perp} \frac{\partial}{\partial v_\perp} v_\perp \mathcal{D} \frac{\partial f}{\partial v_\perp},$$

$$\mathcal{D} = \sum_l \mathcal{D}_0 \, \delta(\omega - l\Omega),$$

where ω is the wave frequency and Ω is the electron cyclotron frequency. Since the Doppler shift effect in $\mathcal{Q}$ is assumed to be negligible ($k_\parallel v_\parallel \simeq 0$), the particle heating is in the perpendicular direction only and, thus, there is no direct resonance heating term in the parallel energy moment equation [45]. The delta function in the quasilinear diffusion coeffcient $\mathcal{D}$ requires that the particles should be resonant somewhere along their orbits to have a nonvanishing $\mathcal{D}$, and its relation to the absorbed wave power will be shown later in this paper.

Due to conservation of magnetic moment along the guiding center motion in a toroidal system, however, the perpendicular heating at the resonance location appears differently along the magnetic field line, resulting in a varying degree of the temperature anisotropy along the magnetic field line. In the present work we calculate the amount of anisotropy at the resonance point for the sake of simplicity.

In order to manipulate the delta function in $\mathcal{D}$, we follow Ref. [49] and expand the resonance condition $l\Omega - \omega = 0$ near the resonance layer whose poloidal angle is given by θ_R,

$$l\Omega - \omega \simeq l \left. \frac{d\Omega}{d\theta} \right|_{\theta=\theta_R} \cdot (\theta - \theta_R) = G \cdot (\theta - \theta_R),$$

where the frequency, G, including the geometrical factor is,

$$G = \omega\epsilon\,\frac{sin\,\theta_R}{1-\epsilon\,cos\,\theta_R},$$

and $B = \dfrac{B_0}{1+\epsilon\,cos\,\theta}$ is used. If D_0 is assumed to be constant [48] with respect to v and λ, the velocity integral of $v_\perp^2 \mathcal{Q}(f)$ becomes

$$\int d^3v\, v_\perp^2 \mathcal{Q}(f) = \frac{4D_0}{G}\int d^3v\ f|_{\theta=\theta_R}.$$

Then, the heating term, *Eq.* (15), is changed into

$$\left\langle \int d^3v\ v_\perp^2 \mathcal{Q}(f)\right\rangle = \frac{4D_0}{G}\,\frac{\pi}{B_m\int \mathcal{J}\,d\theta}\int d\lambda\,dv\,v^2\,\hat{\tau}_b\ f|_{\theta=\theta_R}, \tag{30}$$

and

$$(Heating)_\perp = \frac{4D_0}{G}\,v_e^3\int_0^1 d\lambda\,V_{tt}(\lambda)\int_0^\infty du\,u^2\,f. \tag{31}$$

3.3. Loss and source terms

The ripple-trapped particle fraction, χ, with anisotropic distribution function (see *Fig.* 6) is given as

$$\chi = \frac{\left\langle \int_{ripple\ space} d^3v\, f\right\rangle}{\left\langle \int_{whole\ space} d^3v\, f\right\rangle},$$

and it is a function of ripple strength, δ, and temperature ratio, s. The above integrals can be expressed in terms of (v,λ) and by using *Eq.* (18) for f, yielding

$$\chi\,(s,\delta) = \frac{\displaystyle\int_{\lambda_{min}}^{\lambda_{max}} d\lambda\,\frac{\hat{\tau}_b(\lambda)}{[s-\lambda(s-1)]^{3/2}}}{\displaystyle\int_0^{\lambda_{max}} d\lambda\,\frac{\hat{\tau}_b(\lambda)}{[s-\lambda(s-1)]^{3/2}}}. \tag{32}$$

The upper and lower limit for λ-integral are $\lambda_{max} = B_m/B_{min}$ and $\lambda_{min} = B_m/B_{max}$ where B_{max} and B_{min} are local maximum and minimum magnetic fields provided by external ripple coils. In general, λ_{max} and λ_{min} are functions of inverse aspect ratio, ϵ, and ripple strength, δ. In order to carry out more detailed calculation, we assume that the field ripple is located on top of the plasma where $R = R_0$, and the ripple fields provide a magnetic well. Then $B_{max} \simeq B_0$, and λ_{max} and λ_{min} become

$$\lambda_{min} \simeq \frac{B_m}{B_0} \simeq (1-\epsilon),$$
$$\lambda_{max} \simeq \frac{B_m}{B_0}\frac{B_{max}}{B_{min}} \simeq (1-\epsilon)\left(\frac{1+\delta}{1-\delta}\right).$$

The evaluated ripple-trapped fraction is plotted in *Fig.* 7 with various values of ripple strength, δ.

To complete the loss term, *Eq.* (16), we use

$$\left\{v_\perp^2 v_\parallel^2\right\} = v^2\left\{v_\parallel^2\right\} - \left\{v_\parallel^4\right\},$$

and $\left\{v_\parallel^4\right\}$ is also smoothed to be a polynomial function of λ as

$$V_{tl4}(\lambda) = \frac{\hat{\tau}_b}{v^4}\left\{v_\parallel^4\right\}.$$

Finally, the loss term is expressed as

$$(Loss)_\parallel^\perp = \nu_L\, v_e^5\, \chi(s,\delta) \int_0^1 d\lambda \begin{bmatrix} V_{tp}(\lambda) + V_{tl}(\lambda) - V_{tl4}(\lambda) \\ V_{tl}(\lambda) + V_{tl4}(\lambda) \end{bmatrix} \int_0^\infty du\, u^6 f. \qquad (33)$$

The particle source coefficient η compensating the drift loss is determined by the density conservation. In steady-state, we obtain

$$\eta = \frac{\nu_L}{n_e v_e^2}\chi\left\langle \int d^3v\,\left(v^2 + v_\parallel^2\right) f\right\rangle,$$

and by *Eq.* (11), η is given as

$$\eta = \frac{\nu_L}{n_e v_e^2} v_e^5\, \chi \int_0^1 d\lambda\,(V_{tt}(\lambda) + V_{tl}(\lambda)) \int_0^\infty du\, u^4 f. \qquad (34)$$

Using η in the above form, the source term becomes

$$(Source)_\parallel^\perp = \eta \int_0^1 d\lambda \begin{bmatrix} V_{tp}(\lambda) \\ V_{tl}(\lambda) \end{bmatrix} \int_0^\infty dv\, v^4 f_m,$$
$$= \nu_L\, v_e^5\, \chi(s,\delta)\cdot\frac{3}{8\pi}\begin{bmatrix} 1.244 \\ 0.556 \end{bmatrix} \int_0^1 d\lambda\,(V_{tt}(\lambda) + V_{tl}(\lambda)) \int_0^\infty du\, u^4 f. \qquad (35)$$

3.4. *Evaluation of the temperature anisotropy*

Now, the various terms obtained [Coulomb collision terms, *Eqs.* (26) - (29); wave heating term, *Eq.* (31); loss term, *Eq.* (33); and source term, *Eq.* (35)] are substituted into the two equations (13) and (14) with the warm electron distribution function given by *Eq.* (18). After rearrangements, we get two simultaneous equations to be solved for two unknowns, the temperature ratio s, and the perpendicular energy $m_e\alpha_\perp^2/2$:

$$-\left(T^{\perp}_{pa,e} + Z_{\mathit{eff}}\,T^{\perp}_{pa,i}\right) + \left(-T^{\perp}_{dr,e} + T^{\perp}_{df,e}\right) + \left(\frac{\nu_L}{\nu_0}\right)\chi(s,\delta)\left(-T^{\perp}_{L} + T^{\perp}_{S}\right) + H_\perp = 0, \tag{36}$$

$$\left(T^{\parallel}_{pa,e} + Z_{\mathit{eff}}\,T^{\parallel}_{pa,i}\right) + \left(-T^{\parallel}_{dr,e} + T^{\parallel}_{df,e}\right) + \left(\frac{\nu_L}{\nu_0}\right)\chi(s,\delta)\left(-T^{\parallel}_{L} + T^{\parallel}_{S}\right) = 0. \tag{37}$$

where

$$H_\perp = d_e \int_0^1 d\lambda\, V_{tt}(\lambda) \int_0^\infty du\, u^2 f, \tag{38}$$

$$d_e = \frac{4D_0}{G}\,\frac{1}{\nu_0 v_e^2}, \tag{39}$$

$$T^{\perp}_{pa,e} = T_{11} - T_{12}, \tag{40}$$

$$T^{\perp}_{pa,i} = T_{13} - T_{14}, \tag{41}$$

$$T^{\parallel}_{pa,e} = T_{21} - T_{22}, \tag{42}$$

$$T^{\parallel}_{pa,i} = T_{23} - T_{24}, \tag{43}$$

$$T^{\perp}_{dr,e} = 2\int_0^1 d\lambda\, V_{tp}(\lambda) \int_0^\infty du\, u\, \phi_2(u)\, f, \tag{44}$$

$$T^{\perp}_{df,e} = 2b\int_0^1 d\lambda\, V_{tp}(\lambda)\,(c-\lambda) \int_0^\infty du\, u\, \phi_2(u)\, f, \tag{45}$$

$$T^{\parallel}_{dr,e} = 2\int_0^1 d\lambda\, V_{tl}(\lambda) \int_0^\infty du\, u\, \phi_2(u)\, f, \tag{46}$$

$$T^{\parallel}_{df,e} = 2b\int_0^1 d\lambda\, V_{tl}(\lambda)\,(c-\lambda) \int_0^\infty du\, u\, \phi_2(u)\, f, \tag{47}$$

$$\begin{bmatrix} T^{\perp}_{L} \\ T^{\parallel}_{L} \end{bmatrix} = \int_0^1 d\lambda \begin{bmatrix} V_{tp}(\lambda) + V_{tl}(\lambda) - V_{tl4}(\lambda) \\ V_{tl}(\lambda) + V_{tl4}(\lambda) \end{bmatrix} \int_0^\infty du\, u^6 f, \tag{48}$$

$$\begin{bmatrix} T^{\perp}_{S} \\ T^{\parallel}_{S} \end{bmatrix} = \frac{3}{8\pi} \begin{bmatrix} 1.244 \\ 0.556 \end{bmatrix} \int_0^1 d\lambda\, \left(V_{tt}(\lambda) + V_{tl}(\lambda)\right) \int_0^\infty du\, u^4 f, \tag{49}$$

$$T_{11} = \int_0^1 d\lambda\, \lambda\, V_{tt}(\lambda) \int_0^\infty du\, u\, \phi_1(u)\, \frac{\partial f}{\partial \lambda},$$

$$T_{12} = 2\int_0^1 d\lambda\, \lambda\, V_{tl}(\lambda) \int_0^\infty du\, u\, \phi_1(u) \left(\frac{\partial}{\partial \lambda}\lambda \frac{\partial f}{\partial \lambda} + \frac{1}{2}\frac{\partial f}{\partial \lambda}\right),$$

$$T_{13} = \int_0^1 d\lambda\, \lambda\, V_{tt}(\lambda) \int_0^\infty du\, u\, \frac{\partial f}{\partial \lambda},$$

$$
\begin{aligned}
T_{14} &= 2\int_0^1 d\lambda\,\lambda\,V_{tl}(\lambda)\int_0^\infty du\,u\left(\frac{\partial}{\partial\lambda}\lambda\frac{\partial f}{\partial\lambda}+\frac{1}{2}\frac{\partial f}{\partial\lambda}\right),\\
T_{21} &= 2\int_0^1 d\lambda\,\lambda\,V_{tb}(\lambda)\int_0^\infty du\,u\,\phi_1(u)\,\frac{\partial}{\partial\lambda}\lambda\frac{\partial f}{\partial\lambda},\\
T_{22} &= T_{12},\\
T_{23} &= 2\int_0^1 d\lambda\,\lambda\,V_{tb}(\lambda)\int_0^\infty du\,u\,\frac{\partial}{\partial\lambda}\lambda\frac{\partial f}{\partial\lambda},\\
T_{24} &= T_{14},\\
b &= \frac{s-1}{\alpha_\perp^2/v_e^2},\qquad c=\frac{s}{s-1},\\
\nu_0 &= \frac{3\sqrt{\pi}}{4}\frac{1}{\tau_e},\qquad \frac{1}{\tau_e}=\frac{4\sqrt{2\pi}\,n_e\,e^4\,ln\Lambda}{3\sqrt{m_e}\,(kT_e)^{3/2}}.
\end{aligned}
$$

The first subscripts, *pa*, *dr*, and *df* indicate pitch angle, drag, and diffusion, respectively, and the second subscript after a comma denotes the species of background particles with which warm electrons collide. The integrals in *Eqs.* (40) - (49) are all positive definite since $b \geq 1$ and $c \geq 1$.

Using the definition of the warm particle density,

$$
n_w = \langle\, n(\theta)\,\rangle = \left\langle \int d^3v\, f \right\rangle,
$$

the absorbed wave power can be derived from *Eq.* (30),

$$
\langle P_\perp \rangle = \frac{1}{2} m_e \left\langle \int d^3v\; v_\perp^2\; Q(f) \right\rangle = \frac{m_e}{2}\frac{4D_0}{G}\, n_w.
$$

Therefore, the parameter, d_e which is a function of the wave power and warm particle density is expressed as

$$
d_e = \frac{\langle P_\perp \rangle}{n_w\, kT_e\, \nu_0}. \tag{50}
$$

Because of the functions $\phi_1(u)$ and $\phi_2(u)$, it is not straightforward to evaluate the integrals in *Eqs.* (36) and (37) by hand. Instead, we use the mathematical software, *Mathematica*^{TM} by *Wolfram Research, Inc.* [50] which has the capability of doing symbolic differentiation and integration.

Figure 8 is obtained by solving *Eqs.* (36) and (37), and it depicts the perpendicular and parallel temperatures and their ratio as a function of d_e with various values of ν_L/ν_0, $Z_{eff} = 1$, and $\epsilon = 1/5$. As shown in Ref. [46], one important observation to point out here is that the warm electron temperatures runaway at $d_e \simeq 0.61$ in the absence of a loss mechanism for the tail electrons ($\nu_L/\nu_0 = 0$). This runaway effect

is expected from the fact that the warm particle density, n_w, is kept constant as the wave power is increased. In addition, we used a Maxwellian assumption for the resonant species with no cooling mechanisms other than collisions with the background electrons. The electron energy scattering rate, however, decreases with increasing energy ($\nu_\epsilon \propto v^{-3}$). Hence, for wave power above the runaway power, the validity of the Maxwellian assumption is in doubt. In the presence of a ripple loss term ($\nu_L/\nu_0 \neq 0$), however, this runaway can be avoided. As ν_L/ν_0 increases, the slope of the temperatures at $d_e \simeq 0.61$ becomes smaller. This is because high energy electrons drift out of the region more quickly and thus warm electrons have less probability of becoming runaway electrons. Keeping ν_L/ν_0 fixed, a similar behavior can be found by increasing δ as in *Fig.* 9.

Figure 9 shows an effect of ripple strength on temperature anisotropy. Solid lines are obtained with $\delta = 1\,\%$ and dotted lines are with $\delta = 5\,\%$. As δ increases, more particles are trapped in the ripple region (*Fig.* 7) and thus the drift loss becomes larger, which results in less anisotropy.

Figures 10 through 12 show the calculated anisotropic temperatures for CDX-U case when $\nu_L/\nu_0 = 0.03$ and $\delta = 5\,\%$ with $Z_{eff} = 1, 2, 3, 4$. In general, the behavior is similar to the ion case in the presence of ion cyclotron resonance heating [46]. From these figures, several comments can be made. First, the greater the impurity level is in the plasma (larger Z_{eff}), the higher the $T_\parallel$ (and lower $T_\perp$), and thus less anisotropy is obtained. This is because the pitch angle scattering term increases with Z_{eff} resulting in a more effective spreading of warm electron energy to the parallel direction. Second, as depicted in *Fig.* 11 (*b*), the parallel temperature reaches a maximum value and decreases with d_e. This is because when the wave power is large, the power transferred from the perpendicular to the parallel direction decreases:

$$P_\parallel \sim \nu_\xi\, k \left(T_\perp - T_\parallel\right) \propto \frac{1}{\sqrt{kT_\perp}},$$

where ν_ξ is proportional to $1/v^3$. Third, the parameter d_e is

$$d_i \propto \frac{\langle P_\perp \rangle}{n_w} \frac{\sqrt{m_e k T_e}}{n_e},$$

so that higher anisotropy can be expected at higher background temperature or smaller background density. Fourth, the ratio of perpendicular and parallel temperature reaches as high as 15 and no solution can be obtained beyond a certain value of d_e, which suggest that there exists a critical wave power above which our bi-Maxwellian picture does not hold. In order to extend the present analysis above this critical power, a better description of the distribution for warm species may be necessary.

The present study shows that the temperature anisotropy can be made quite large by putting the electron cyclotron resonance layer in the ripple region. Thus, the ripple-trapped fraction of the warm electrons can be significant. For example, for $\delta = 5\,\%$ and $T_\perp/T_\| = 10$, *Fig.* 7 yields $\chi \approx 25\,\%$. A significant number of warm electrons can drift to smaller minor radial positions to create a negative electrostatic potential (ripple injection).

4. SIMULATION OF ENERGETIC ELECTRON ORBITS AND RADIAL ELECTRIC FIELD GENERATION

In order to understand the behavior of a suprathermal electron with $v_\perp / v_\| \gg 1$ in ripple fields, a guiding-center orbit simulation has been attempted. The computer code numerically integrates four guiding-center equations of motion using the fourth-order Runge-Kutta method in the presence of ripple fields in a tokamak geometry. Equations of motion to be solved are:

$$\begin{aligned}
\frac{dR}{dt} &= (v_d)_R + v_\| \frac{B_R}{B}, \\
R\frac{d\phi}{dt} &= (v_d)_\phi + v_\| \frac{B_\phi}{B}, \\
\frac{dZ}{dt} &= (v_d)_Z + v_\| \frac{B_Z}{B}, \\
\frac{dv_\|}{dt} &= -\frac{\mu}{m_e}\frac{dB}{d\ell},
\end{aligned}$$

where μ is the magnetic moment and (B_R, B_ϕ, B_Z) are components of magnetic fields. The drift velocity, v_d, is a combination of ∇B drift and curvature drift as given in *Eq.* (4), and $\mathbf{E} \times \mathbf{B}$ drift. An energetic test electron is subject to Coulomb drag and pitch-angle scattering off the background electrons, ions, and impurity ions. This process is described in the code by the Langevin equations,

$$\begin{aligned}
\frac{dv}{dt} &= -\frac{\nu_\epsilon}{2}v, \\
\frac{dv_\|}{dt} &= -\nu_\xi v_\|,
\end{aligned}$$

with the pitch-angle scattering rate ν_ξ and the energy slowing down rate ν_ϵ. At each time step, the energetic electron's pitch angle is altered by means of random number generator. The simulation assumes concentric flux surfaces for simplicity.

The major and minor radius of CDX-U device are $0.35\,m$ and $0.22\,m$, respectively with a natural elongation ($\kappa \simeq 1.5$). Some values used in the simulation are $\overline{T}_e = 100\,eV$, $\overline{n}_e = 2 \times 10^{18}\,m^{-3}$, $q(a) = 4$, and $B_0 = 0.1\,T$.

Figures 13 and 14 are cross-sectional and top views of an energetic electron orbiting under the influence of ripple fields. For these figures, the ripple coil current is $I_{rip} = 8\,kA\cdot turn$, giving a ripple strength of $\delta = 2.82\,\%$ at the starting point ($R = 0.39\,m$, $\phi = 0\,°$, $Z = 0.30\,m$) which is marked by an asterisk. It is assumed that the energetic electron initially has most of its kinetic energy in the direction perpendicular to the magnetic field. The toroidal field is pointed counterclockwise when viewed from the top. The ∇B drift direction is downward for electrons. As shown in the figures, the energetic electron is locally trapped toroidally in the ripple well for about 4 μsec while experiencing downward drifts. Due to the decrease of the ripple strength and an increase of Coulomb collisions as it moves toward plasma center (increasing $n_e(r)$), the ripple-trapped electron now becomes detrapped and moves in the toroidal direction. The electron follows a banana orbit and, at the same time, it loses its energy to background particles by Coulomb drag. The elapsed time from the initial energy of $1.5\,keV$ to the final energy of $0.5\,keV$ is $74\,\mu sec$. As shown in *Fig.* 13, the electron penetrates $0.13\,m$ into the plasma.

The radial penetration depth of an energetic electron can be controlled by two independent parameters, ripple strength and the initial electron energy. Four different cases are compared in *Fig.* 15 where (a) $I_{rip} = 4\,kA\cdot turn$ ($1.45\,\%$ at the starting point) and $W_0 = 0.7\,keV$, (b) $I_{rip} = 4\,kA\cdot turn$ ($1.45\,\%$) and $W_0 = 2.0\,keV$, (c) $I_{rip} = 10\,kA\cdot turn$ ($3.50\,\%$) and $W_0 = 0.7\,keV$, (d) $I_{rip} = 8\,kA\cdot turn$ ($2.82\,\%$) and $W_0 = 1.0\,keV$. As can be seen from the figure, in order to produce a similar penetration depth to that in (d), either higher particle energy (from (a) and (b)) or larger ripple strength (from (a) and (c)) is necessary to get a sufficient penetration.

Since these penetrated electrons accumulate at the flux surfaces where they are detrapped from the ripple region and thermalized, the net effect is to charge the plasma negatively resulting in a build-up of electrostatic potentials, i.e., radial electric fields (E_r) from the edge toward the plasma center with a scale length of the penetration distance. In order to simulate this phenomenon, a few assumptions are made. First, the plasma is divided into a number of radial zones separated by concentric flux surfaces. The background particle density and temperature are assumed to be constant on a flux surface due to large parallel heat conduction [51] ($\kappa_{\|}/\kappa_{\perp} \sim (\omega\tau)^2 \gg 1$). Second, in order to speed up the numerical procedure, we assume that a single electron deposits multiple charges (for example, $Q = -10^{12}\,e$) at the flux surface where detrapping occurs. Third, it is also assumed that a series of electrons are launched sequentially at the same starting point under the same condition. (The algorithm for the calculation of radial electric fields is found in *Fig.* 16). In this way, the n^{th} launched electron sees the electric fields generated by 1^{st} to $(n-1)^{th}$ electrons, and it experiences $\mathbf{E} \times \mathbf{B}$ drifts in both poloidal and toroidal directions.

Since the injected warm electrons move radially inward and accumulate at flux surfaces farther inward than the initial flux surface where energetic electrons start their drifts, the background electron current has to counter-balance the injected electron current in steady-state. The outward radial current carried by the background cold electrons induced by an inward electric field can be written in the form

$$E_r - E_{r0} = \frac{1}{\sigma_\perp}\, j_r, \tag{51}$$

where E_{r0} is the equilibrium electric field without j_r and $\sigma_\perp$ is the electrical conductivity orthogonal to the flux surfaces, which may be a function of E_r. In order to find out E_r from a given j_r, we use the force balance relation between the $j_r \times B_\phi$ force and the plasma viscous force in the poloidal direction.

$$j_r\, B_\phi = (\nabla \cdot \Pi)_\theta, \tag{52}$$

where Π is the viscosity tensor and j_r is the radially outward electrical current carried by the background plasma. Reference [52] has been used for a simple analytic expression of the viscosity tensor Π. As the electric field increases, the $\mathbf{E} \times \mathbf{B}$ rotation speed v_E increases. At low v_E values, $(\nabla \cdot \Pi)_\theta$ increases with v_E. Hence, for a given j_r, an equilibrium value of v_E is determined. As v_E is increased further, $(\nabla \cdot \Pi)_\theta$ reaches a maximum and then decreases [52]. In this case, there can be two solutions for v_E, leading to a bifurcation. In a steady-state, the outward plasma current j_r will have to balance the injected current. *Equation* (52) is another way of writing *Eq.* (51).

Figure 17 shows a time trace of radial profiles of electric fields generated by 100 electrons and the corresponding final rotation speed v_E assuming poloidal rotation is dominant. The dotted curve in *Fig.* 17 (a) indicates the radial electric field strength above which a bifurcation occurs. The shape of E_r which looks similar to that observed in other devices with different methods [53, 54] is not only determined by the electron deposition profile but also by the information of background particles via $\sigma_\perp$ of *Eq.* (51). The time elapsed to induce $-3.0\,kV/m$ is less than $0.4\,msec$. Since the deposited charge per electron was assumed to be $Q = -4.6 \times 10^{12} e$ and 100 electrons were launched for the calculation, the total number of energetic electrons involved is 4.6×10^{14}. This indicates that the injection of a population of electrons equal to

1.2% of the total population between $r/a = 0.9$ and $r/a = 1.0$ is necessary to generate $-3.0\,kV/m$ of electric fields. For this particular run (*Fig.* 17), the total injected radial current is $23\,A$ and this is realized approximately by the electrical charge of $4.6 \times 10^{14}e$ and the average detrapping time of $3\,\mu sec$. This amount of radial current suggests that only $23\,kW$ of electron cyclotron heating power may be required for a bifurcation to occur.

A large Q-value produces large electric fields but once E_r reaches a certain amount, launched electrons become less penetrating due to larger $\mathbf{E} \times \mathbf{B}$ drifts. Shown in *Fig.* 18 (a) are the radial electric field profiles generated by 10, 20, 30, 40, 50, 60, 80, and 100 electrons. The incremental increase in E_r becomes smaller with each injected electron, suggesting the saturation of E_r at some limit. In (b), the radial position at which detrapping occurs is plotted.

The role of radial electric fields on orbits of successive electrons is illustrated in *Figures* 19 and 20. Compared to the case without radial electric fields (*Fig.* 19 (a)), the cases with nonzero E_r makes electrons less penetrative as seen in *Fig.* 19 (b). *Figure* 20 is an illustration to show the effect of E_r on the electron penetration where the orbits of four different ($1^{st}, 22^{nd}, 48^{th}$ and 100^{th}) electrons among 100 launched electrons are plotted. It shows the shift of orbits in the direction of the $\mathbf{E} \times \mathbf{B}$ drift whose poloidal component is in the clockwise direction in the figure.

In *Fig.* 21, the electric field profile is shown with several different ripple strengths. As is seen in the figure, the electric field can be maximized at $r/a \simeq 0.86$ with a modest amount of ripple strength ($I_{rip} = 4\,kA\cdot turn$). On the other hand, with larger ripple fields, E_r propagates further radially inward (due to deeper penetration) while the peak value is decreased (due to the larger detrapping time and thus, smaller radial current density injected).

As discussed previously, there is another parameter that can be used to control the electron penetration depth and, thus, E_r. *Figure* 22 shows that a fairly large amount of E_r can be obtained by increasing the initial energy of energetic electrons for a given ripple strength and Q.

5. SUMMARY AND DISCUSSION

For larger size future devices such as ITER, obtaining H-mode is very important [55, 56] especially for an adequate ignition margin and the possibility of using ELMs to facilitate ash removal [57]. In this context, it may be meaningful to extend this electron ripple injection concept to an active control of plasma confinement via externally generated radial electric fields. In order to estimate the required

ECRH power in ITER, a similar simulation has been performed with ITER parameters ($\overline{n}_e$=$2 \times 10^{19}\, m^{-3}$, $\overline{T}_e$=$3.7\, keV$, $a = 3.0\, m$, $\kappa = 1.54$, $R_0 = 8.1\, m$, $B_0 = 5.7\, T$, $q(a) = 2.85$, $Z_{eff} = 1.34$). It is assumed that the ripple coils are located at $R = R_0$ and $Z = 1\, m$ above the edge of the plasma with the coil current of $0.8\, MA$. Since the critical electron energy above which our assumptions are valid is given by $62\, keV$ (*Eq.* (8)), the energetic electrons are launched with the energy of $80\, keV$ at $R = R_0$, $Z = 0.2\, m$ below the edge of the plasma where the ripple strength is 0.73 %. *Figure* 23 is obtained from 100 electrons assuming $Q = -2.0 \times 10^{15} e$ and it shows the electric field profile and the corresponding poloidal rotation velocity profile. In order to produce approximately $-260\, kV/m$ of electric fields, the total injected radial current is calculated to be $120\, A$ and the time needed is $11.9\, msec$. This would mean approximately $10\, MW$ of ECRH power is required to induce an E_r-bifurcation, which is relatively modest for ITER. For this case, a total of 2.0×10^{17} electrons are needed and this is a negligible portion of ITER edge electrons.

The electron ripple injection concept can be a promising non-intrusive source of strong radial electric field to possibly control the tokamak plasma edge transport by inducing the plasma into improved confinement plasma regimes, i.e., L-H and H-VH mode. ECRH is utilized in an electron ripple injector to increase the ripple-trapped particle fraction and electron heating, and anisotropic temperatures of the epithermal electrons are calculated using a bi-Maxwellian distribution function. Results show that $T_\perp/T_\|$ can be quite large with a moderate wave power input and a reasonable ripple strength. The behavior of energetic electrons and the generation of radial electric field in the presence of externally-provided ripple fields are investigated by a Monte-Carlo guiding-center electron orbit code. A series of simulations predicts that the generation of a fairly large radial electric field via ERI technique is possible not only on CDX-U but also on a reactor size device, ITER, with a reasonable power of about $23\, kW$ and $10\, MW$, respectively. This prediction is an encouraging result suggesting that the ERI technique could be a promising alternative for generating a strong radial electric field and, thus, for possibly controlling tokamak plasma transport. An experimental investigation of this subject can be worthwhile in the near future.

6. ACKNOWLEDGEMENT

The authors wish to thank Dr. D.S. Darrow for helpful discussions. One of the authors (W. Choe) wishes to thank Dr. H. Towner for making some of his Fortran subroutines available for the present calculation. This work was supported by the

United States Department of Energy under Contract No. DE-AC02-76-CH0-3073 and Grant No. DE-FG02-86-ER53223.

References

[1] WAGNER, F., BECKER, G., BEHRINGER, K., et al., Phys. Rev. Lett. **49** (1982) 1408.

[2] TAYLOR, R.J., BROWN, M.L., FRIED, B.D., et al., Phys. Rev. Lett. **63** (1989) 2365.

[3] ASKINAZI, L.G., GOLANT, V.E., LEBEDEV, S.V., et al., Nucl. Fusion **32** (1992) 271.

[4] WEYNANTS, R.R.,TAYLOR, R.J., VANDENPLAS, P.E., et al., in Controlled Fusion and Plasma Physics (Proc. 17th Eur. Conf. Armsterdam, 1990), Vol. 14B, Part I, European Physical Society, Geneva (1990) 287.

[5] ODAJIMA, K., et al., in Plasma Physics and Controlled Nuclear Fusion Research 1986 (Proc. 11th Int. Conf. Kyoto, 1986), Vol. 1, IAEA, Vienna (1987) 151.

[6] TANGA, A., BARTLETT, D.V., BEHRINGER, K., et al., in Plasma Physics and Controlled Nuclear Fusion Research 1986 (Proc. 11th Int. Conf. Kyoto, 1986), Vol. 1, IAEA, Vienna (1987) 65.

[7] VAN NIEUWENHOVE, R., et al, in Controlled Fusion and Plasma Physics (Proc. 18th Eur. Conf. Berlin, 1991), Vol. 15C, Part I, European Physical Society, Geneva (1991) 405.

[8] COUTURE, P., BOILEAU, A., DÉCOSTE, R., et al., Phys. Lett. A **163** (1992) 204.

[9] PHILLIPS, P.E., WOOTTON, A.J., ROWAN, W.L., et al., J. Nucl. Mat. **145-147** (1987) 807.

[10] SAUTHOFF, N., ASAKURA, N., BELL, R., et al., in Plasma Physics and Controlled Nuclear Fusion Research 1990 (Proc. 13th Int. Conf. Washington, 1990), Vol. 1, IAEA, Vienna (1991) 709.

[11] MATSUMOTO, H., FUNAHASHI, A., HASEGAWA, M., et al., in Controlled Fusion and Plasma Physics (Proc. 14th Eur. Conf. Madrid, 1987), Vol. 11D, Part I, European Physical Society, Geneva (1987) 5.

[12] TOI, K., et al., in Controlled Fusion and Plasma Physics (Proc. 16th Eur. Conf. Venice, 1989), Vol. 13B, Part I, European Physical Society, Geneva (1989) 221.

[13] BURRELL, K., ALLEN, S.L., BRAMSON, G., et al., Plasma Phys. Controll. Fusion **31** (1989) 1649.

[14] BUSH, C.E., GOLDSTON, R.J., SCOTT, S.D., et al., Phys. Rev. Lett. **65** (1990) 424.

[15] BUSH, C.E., BRETZ, N., BUDNY, R., et al., Plasma Phys. Controll. Fusion **36** (1994) 153.

[16] LOHR, J., STALLARD, B.W., PRATER, R., et al., Phys. Rev. Lett. **60** (1988) 2630.

[17] HOSHINO, K., YAMAMOTO, T., KAWASHIMA, H., et al., Phys. Rev. Lett. **63** (1989) 770.

[18] ERCHMANN, V., BRAKEL, R., BURHENN, R., et al., in Plasma Physics and Controlled Nuclear Fusion Research 1992 (Proc. 14th Int. Conf. Würzburg, 1992), Vol. 2, IAEA, Vienna (1993) 469.

[19] ERCHMANN, V., WAGNER, F., BALDZUHN, J., et al., Phys. Rev. Lett. **70** (1993) 2086.

[20] STEINMETZ, K., NOTERDAEME, J.-M., WAGNER, F., et al., Phys. Rev. Lett. **58** (1987) 124.

[21] TSUJI, S., USHIGUSA, K., IKEDA, Y., et al., Phys. Rev. Lett. **64** (1990) 1023.

[22] OSBORNE, T.H., BROOKS, N.H., BURRELL, K.H., et al., Nucl. Fusion **30** (1990) 2023.

[23] KAUFMANN, M., BOSCH, H.-S., FIELD, A., et al., Plasma Phys. Controll. Fusion **35** (1993) 205.

[24] CAROLAN, P.G., FIELDING, S.J., GERASIMOV, S., et al., Plasma Phys. Controll. Fusion **36** (1994) 111.

[25] SNIPES, J.A., GRANETZ, R.S., GREENWALD, M., et al., Nucl. Fusion **34** (1994) 1039.

[26] GROEBNER, R.J., BURRELL, K.H., SERAYDARIAN, R.P., et al., Phys. Rev. Lett. **64** (1990) 3015.

[27] GROEBNER, R.J., BURRELL, K.H., GOHIL, P., et al., Rev. Sci. Instrum. **61** (1990) 2920.

[28] GROEBNER, R.J., PEEBLES, W.A., BURRELL, K.H., et al., in Plasma Physics and Controlled Nuclear Fusion Research 1990 (Proc. 13th Int. Conf. Washington, 1990), Vol. 1, IAEA, Vienna (1991) 453.

[29] IDA, K., HIDEKUMA, S., MIURA, Y., et al., Phys. Rev. Lett. **65** (1990) 1364.

[30] IDA, K., HIDEKUMA, S., KOJIMA, M., et al., Phys. Fluids B **4** (1992) 2552.

[31] JACKSON, G.L., WINTER, J., TAYLOR, T.S., et al., Phys. Rev. Lett. **67** (1991) 3098.

[32] TAYLOR, T.S., OSBORNE, T.H., BURRELL, K.H., et al, in Plasma Physics and Controlled Nuclear Fusion Research 1992 (Proc. 14th Int. Conf. Würzburg, 1992), Vol. 1, IAEA, Vienna (1993) 167.

[33] GREENFIELD, C.M., BALET, B., BURRELL, K.H., et al., Plasma Phys. Controll. Fusion **35** (1993) B263.

[34] BURRELL, K.H., DOYLE, E.J., GOHIL, P., et al., Phys. Plasmas **1** (1994) 1536.

[35] OSBORNE, T.H., BURRELL, K.H., CARLSTROM, T.N., et al., Plasma Phys. Controll. Fusion **36** (1994) A237.

[36] OSBORNE, T.H., BURRELL, K.H., CARLSTROM, T.N., et al., Nucl. Fusion **35** (1995) 23.

[37] JET TEAM, Plasma Phys. Controll. Fusion **36** (1994) A23.

[38] BIGLARI, H., et al., Phys. Fluids B **2** (1990) 1.

[39] SHAING, K.C., et al., Phys. Fluids B **2** (1990) 1492.

[40] "ITER Conceptual Design Report", ITER Documentation Series, No. 18 (International Atomic Energy Agency, Vienna, 1991).

[41] ONO, M., FURTH, H., FOREST, C.B., et al., US/Japan Workshop on Edge Plasma Modification in Fusion Plasmas, Nagoya, Japan, 1990.

[42] CHOE, W., ONO, M., HWANG, Y.S., Proc. of IAEA Technical Committee Meeting on Tokamak Plasma Biasing, Montreal, Sep. 1992.

[43] GOLDSTON, R.J., JASSBY, D.L., TOWNER, H.H., et al., Proc. 7th Symposium on Engineering Problems of Fusion Research, vol. 2, (1977) 1333.

[44] STRINGER, T.E., Nucl. Fusion **12** (1972) 689.

[45] KENNEL, C.F., ENGELMANN, F., Phys. Fluids **9** (1966) 2377.

[46] CHOE, W., CHANG, C.S., ONO, M., Phys. Plasmas **2** (1995) 2044.

[47] CHANG, C.S., LEE, J-Y., WEITZNER, H., Phys. Fluids B **3** (1991) 3429.

[48] CHANG, C.S., COLESTOCK, P., Phys. Fluids B **2** (1990) 310.

[49] STIX, T.H., Nucl. Fusion **15** (1975) 737.

[50] WOLFRAM, S., *Mathematica*, Second Edition, Addison-Wesley, 1991.

[51] BRAGINSKII, S.I., in Review of Plasma Physics Vol.1 (ed. M.A. Leontovich), p.228, Consultants Bureau, New York.

[52] CHANG, C.S., Phys. Fluids B **5** (1993) 4360.

[53] IDA, K., KAWAHATA, K., TOI, K. , et al., Nucl. Fusion **31** (1991) 943.

[54] KIM, J., BURRELL, K.H., GOHIL, P., et al., Phys. Rev. Lett. **72** (1994) 2199.

[55] PERKINS, F., BARABASCHI, P., BOSIA, G., et. al., will appear in Plasma Physics and Controlled Nuclear Fusion Research 1994 (Proc. 15th Int. Conf. Seville, 1994), IAEA, Vienna (1995).

[56] KAYE, S., and the ITER Joint Central Team and Home Teams, will appear in Plasma Physics and Controlled Nuclear Fusion Research 1994 (Proc. 15th Int. Conf. Seville, 1994), IAEA, Vienna (1995).

[57] HILLIS, D.L., HOGAN, J.T., WADE, M.R., et al., in Plasma Physics and Controlled Nuclear Fusion Research 1992 (Proc. 14th Int. Conf. Würzburg, 1992), Vol. 1, IAEA, Vienna (1993) 577.

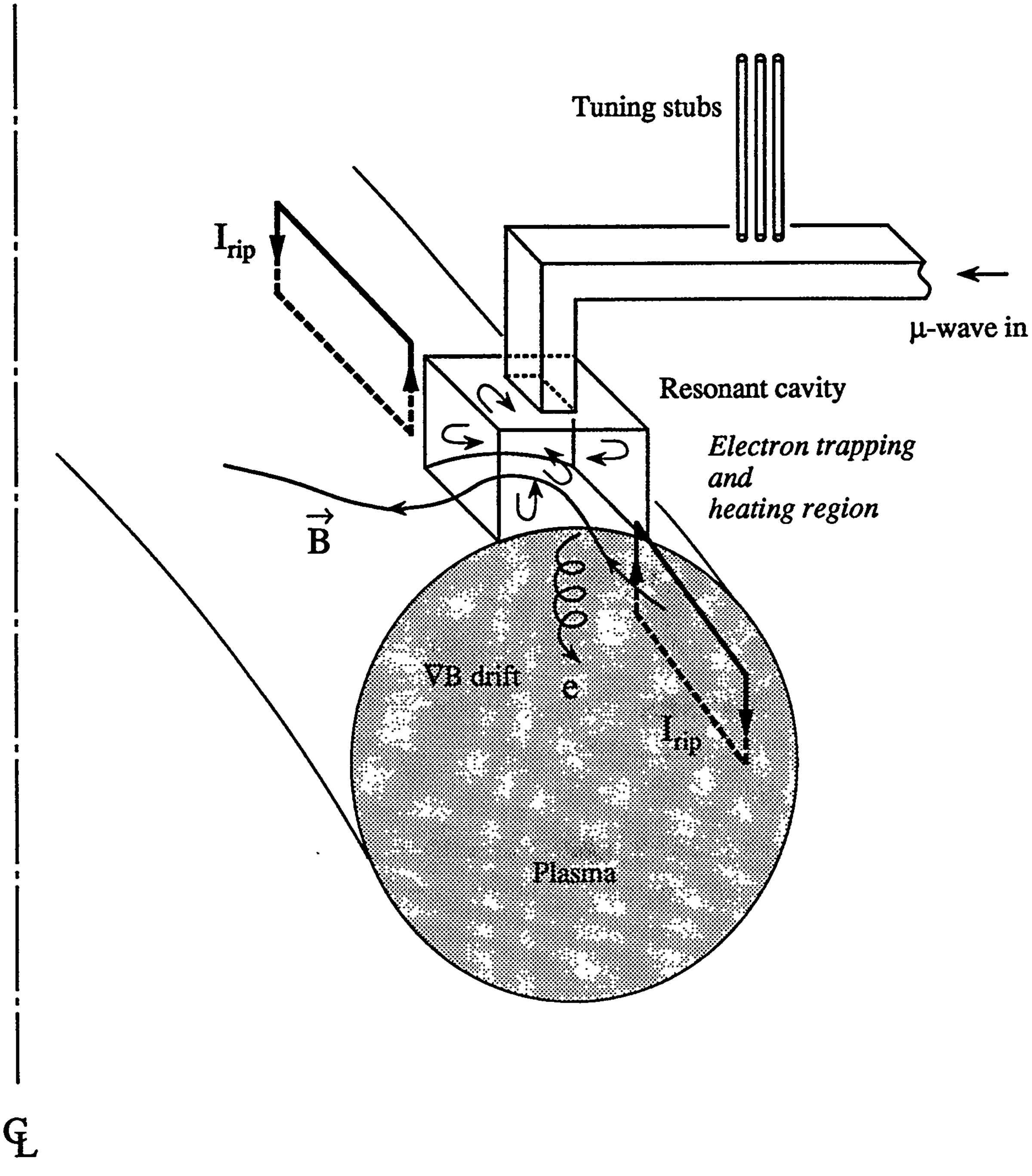

Figure 1: Schematic of the electron ripple injector.

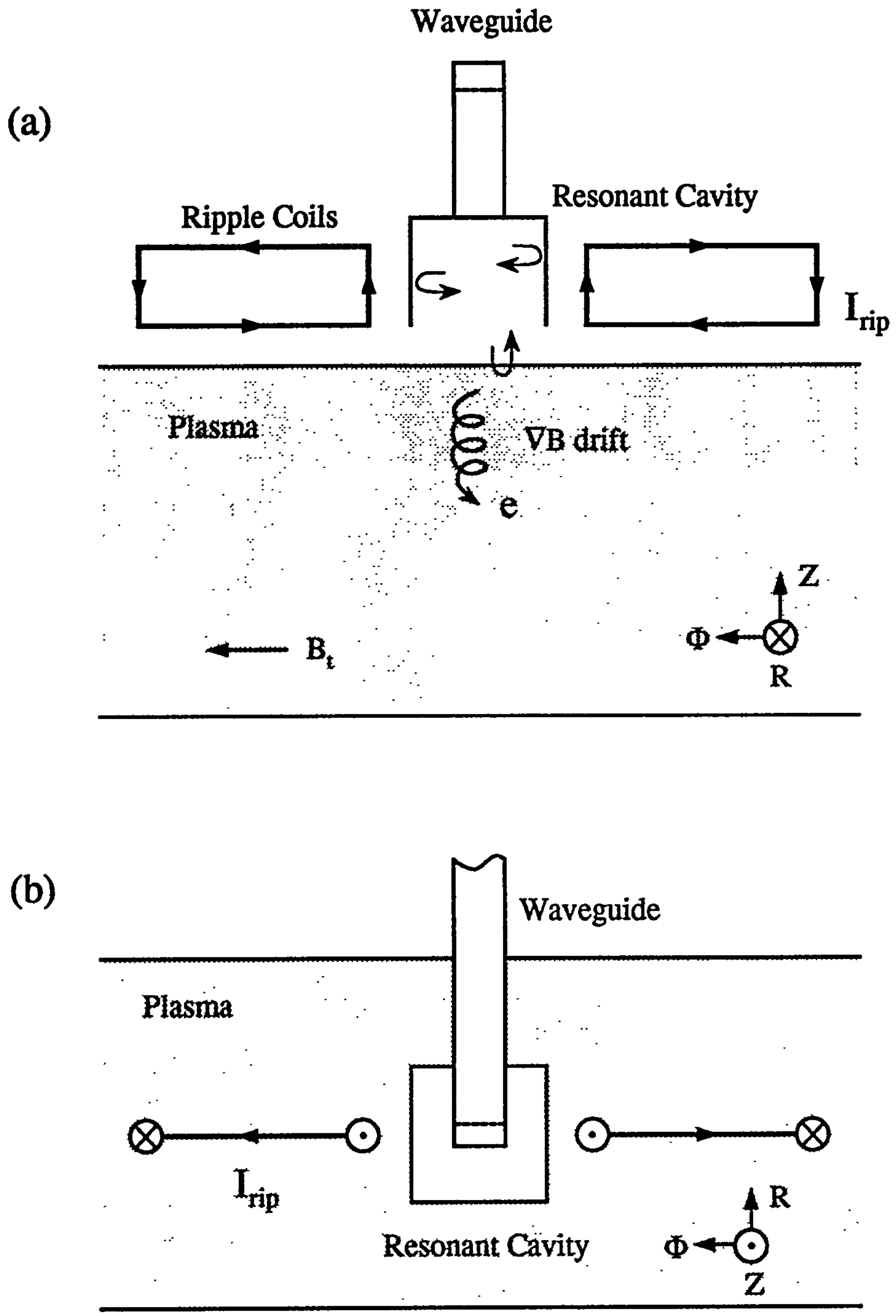

Figure 2: Schematic of the electron ripple injector (a) seen from the major axis, and (b) viewed from the top of a tokamak plasma.

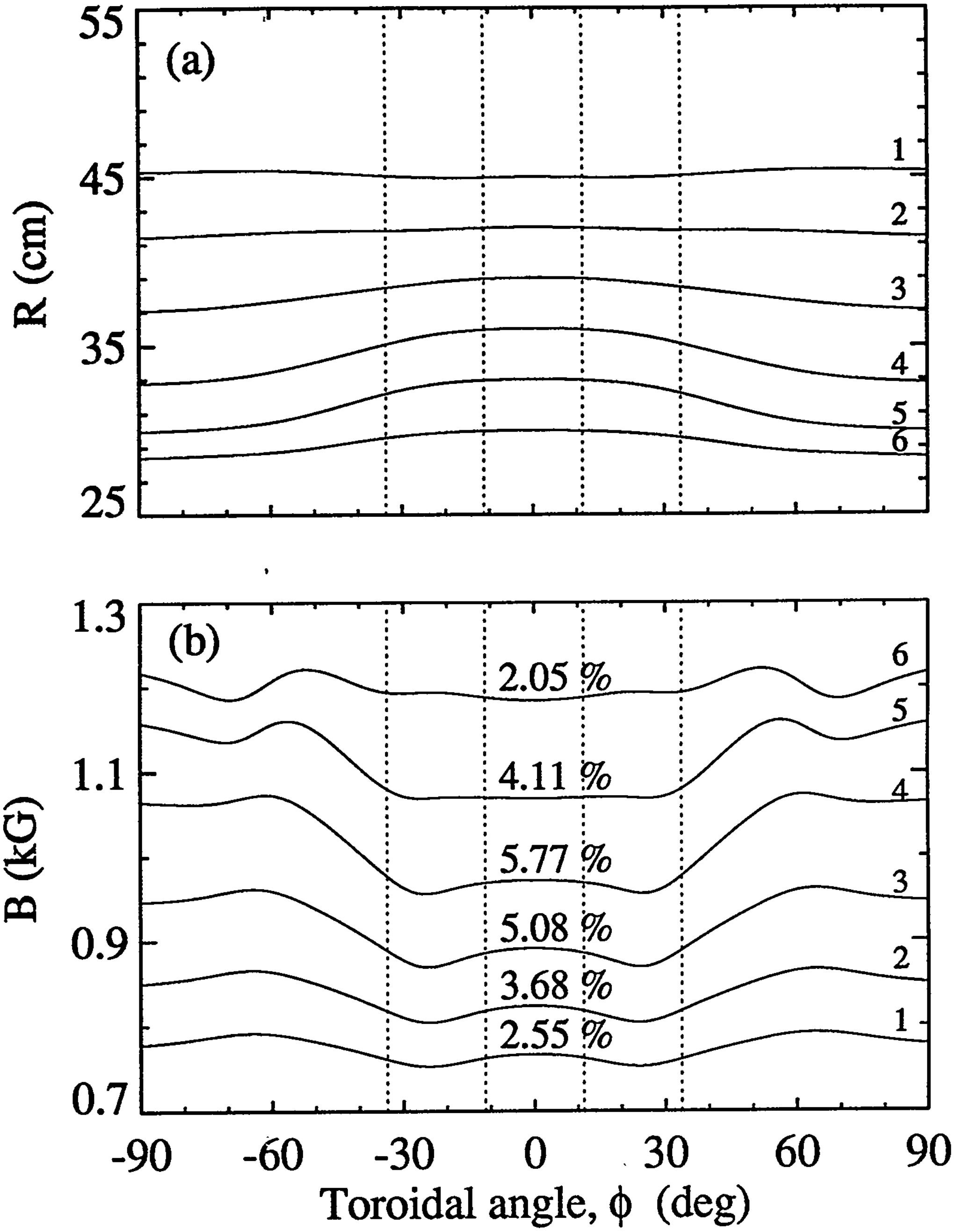

Figure 3: Magnetic field lines at different radial positions but at $Z = 33\,cm$ where $\mathbf{B} = \mathbf{B}_{TF} + \mathbf{B}_{rip}$. Ripple coils are aligned as in *Fig.* 1 and are assumed to be located at $R = 35\,cm$, $Z = 42\,cm$. $I_{rip} = 10\,kA\cdot turn$. Shown in the middle of (b) is magnetic field ripple strength of each field line. Dotted lines indicate the toroidal location of ripple coils.

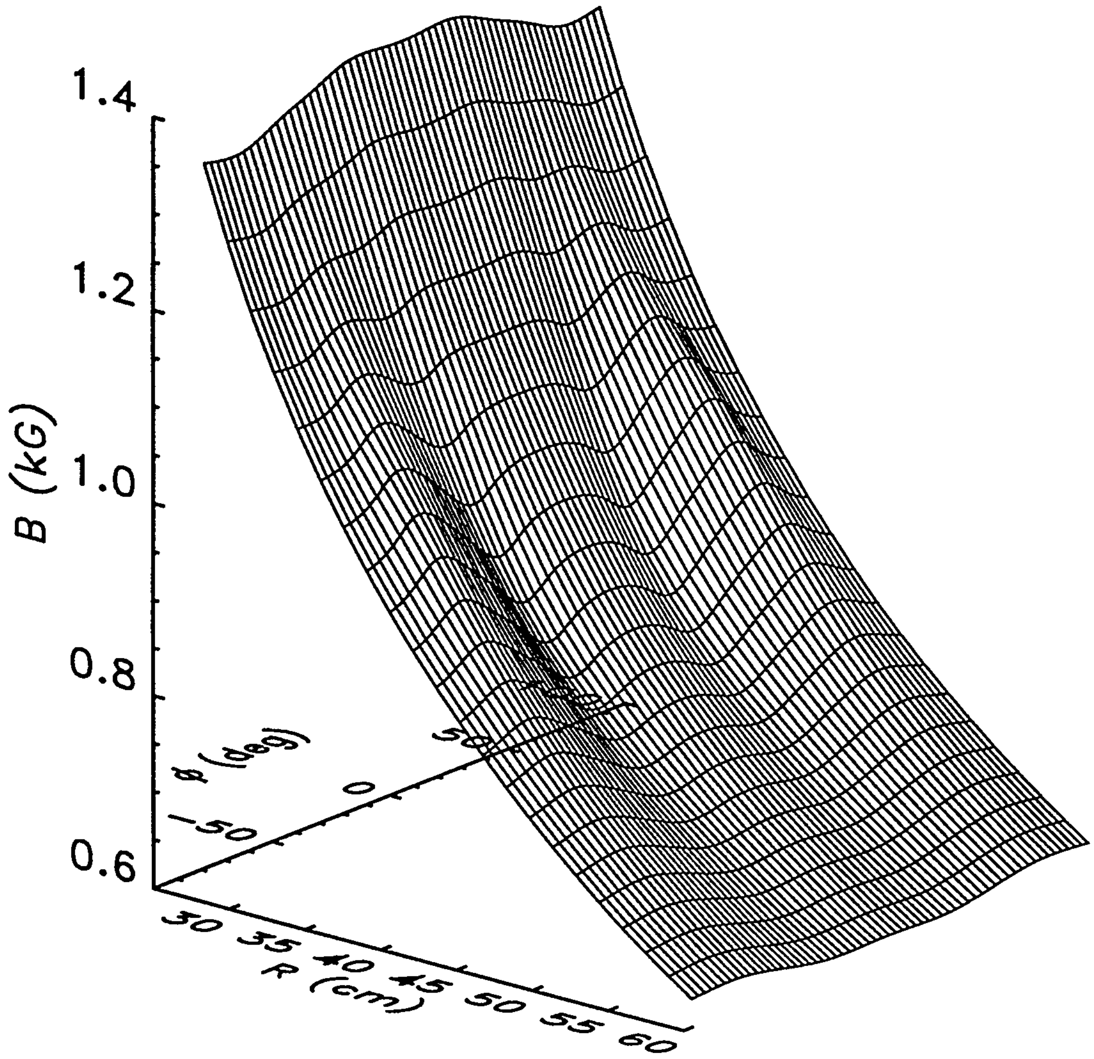

Figure 4: 3-dimensional plot of magnetic field strength at $Z = 33\,cm$ with $I_{rip} = 10\,kA\cdot turn$. $1/R$-dependence by toroidal field is seen and local magnetic well is created by ripple coils.

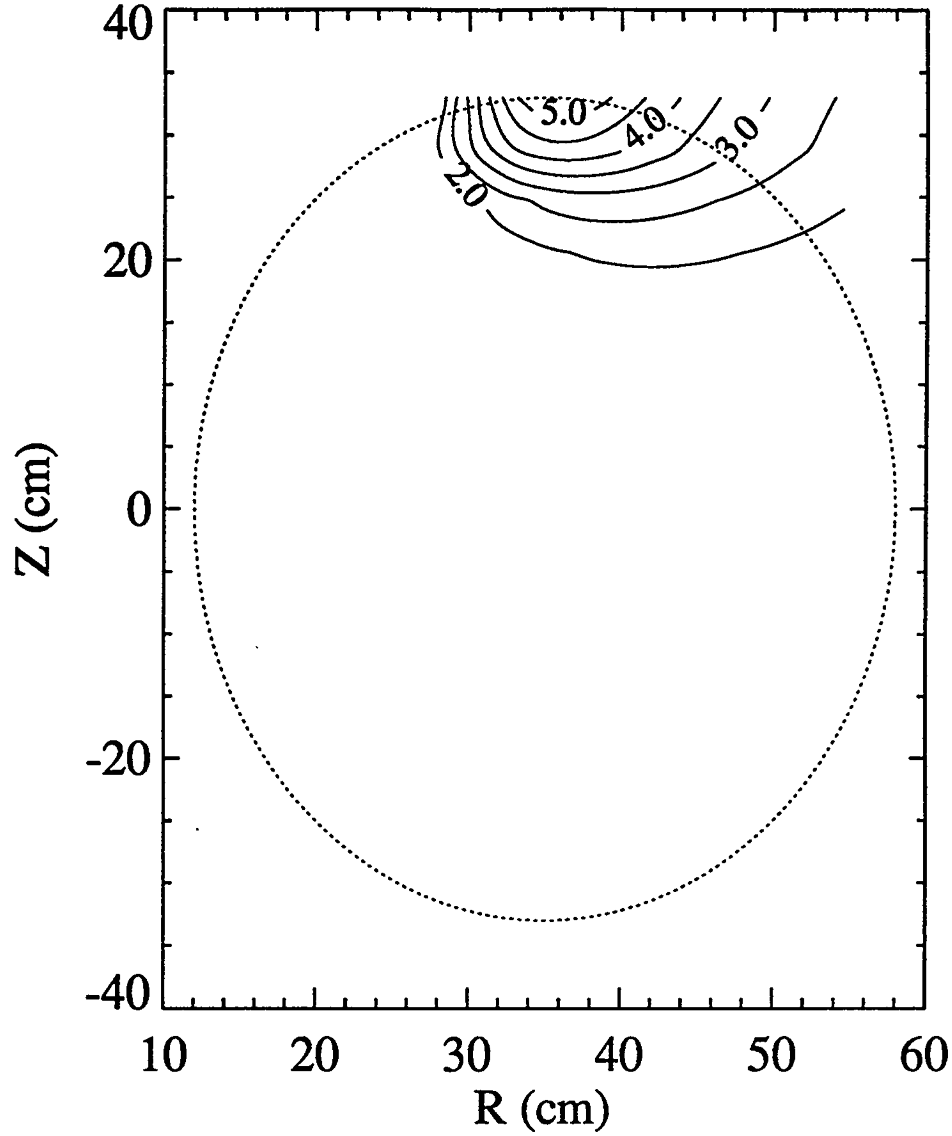

Figure 5: Contour plot of field ripple strength with toroidal angle of 25° from the center of ripple coils. Dotted line depicts the plasma region. $I_{rip} = 10\,kA \cdot turn$.

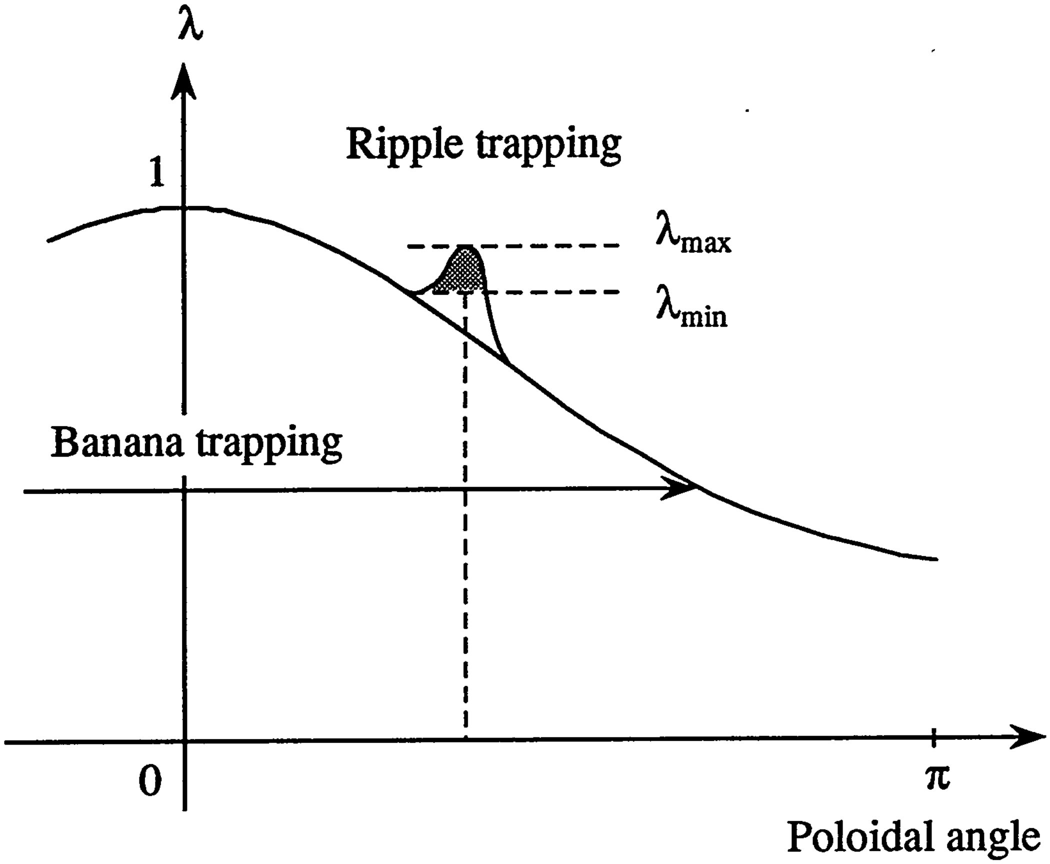

Figure 6: Region of λ for ripple trapping.

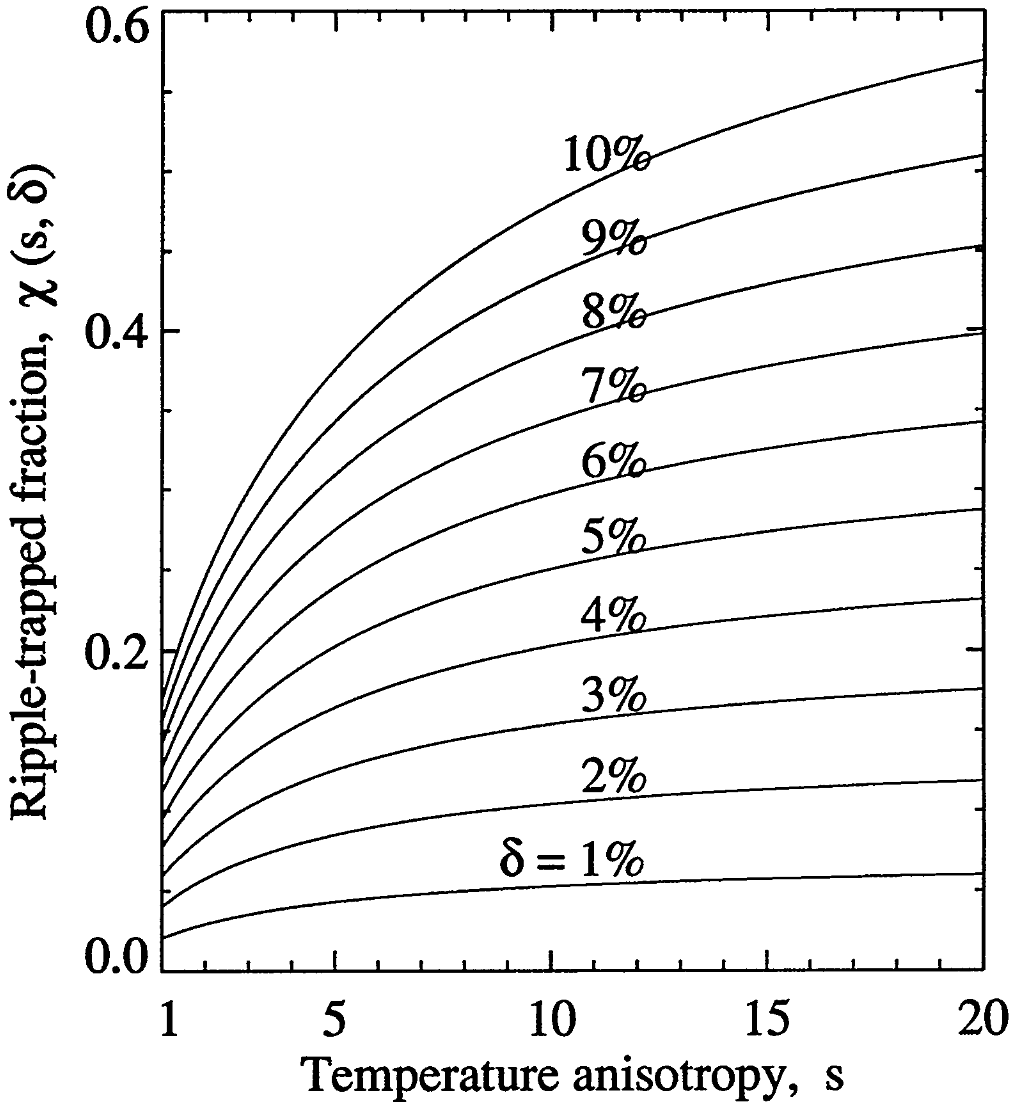

Figure 7: The fraction of trapped electrons in the magnetic ripple fields as a function of temperature anisotropy, s, and ripple fraction, δ.

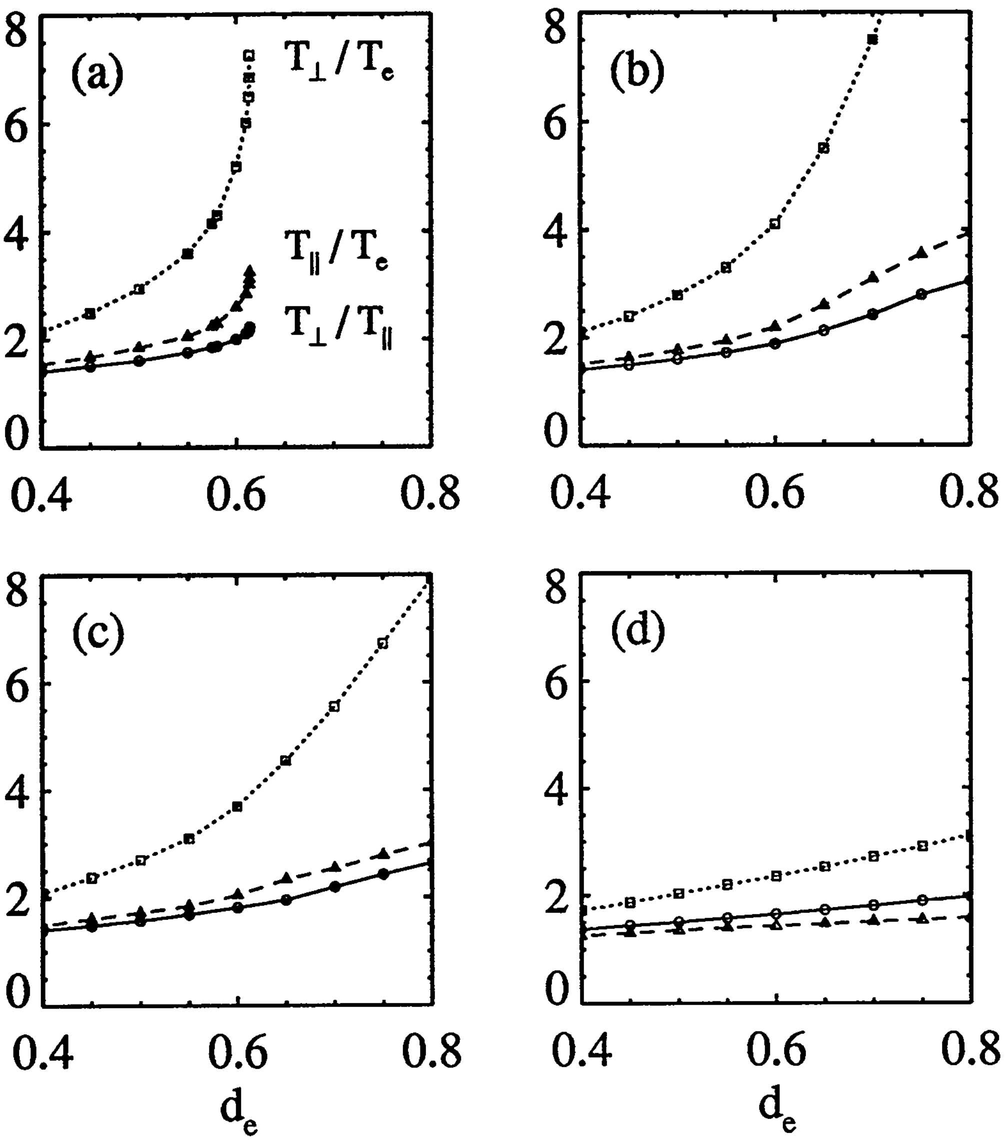

Figure 8: Temperatures with various ν_L. (a) $\nu_L/\nu_0 = 0$, (b) $\nu_L/\nu_0 = 0.005$, (c) $\nu_L/\nu_0 = 0.01$, and (d) $\nu_L/\nu_0 = 0.1$. When $\nu_L/\nu_0 = 0$, temperatures increase very rapidly at $d_e \simeq 0.61$ indicating run-away. $\delta = 5\,\%$ and $Z_{eff} = 1$.

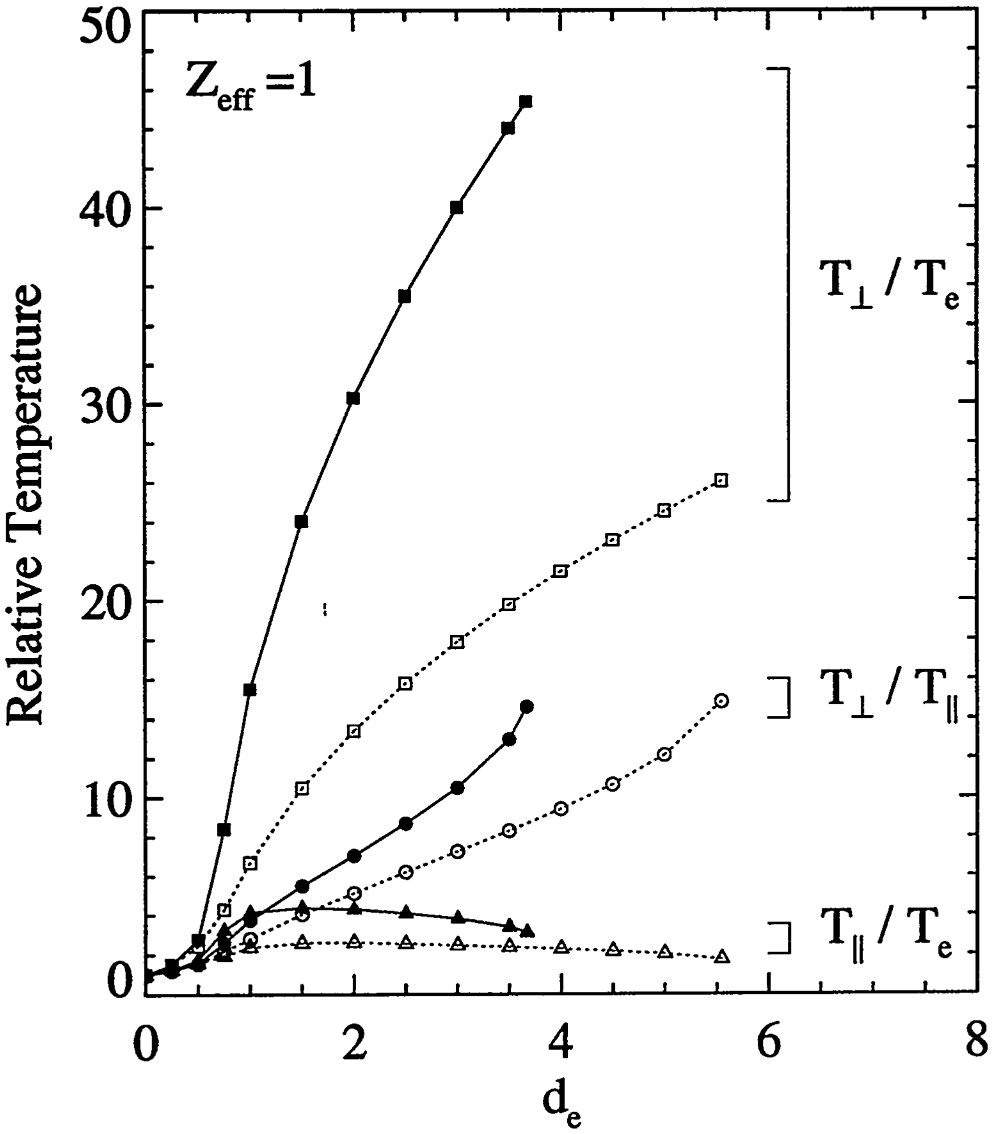

Figure 9: Temperature anisotropy with different ripple strength. Solid lines indicate the case with $\delta = 1\,\%$ and dotted lines with $\delta = 5\,\%$. With a larger ripple fraction, more particles are trapped and are lost resulting in less temperature anisotropy at fixed d_e. $\nu_L/\nu_0 = 0.03$ and $Z_{eff} = 1$.

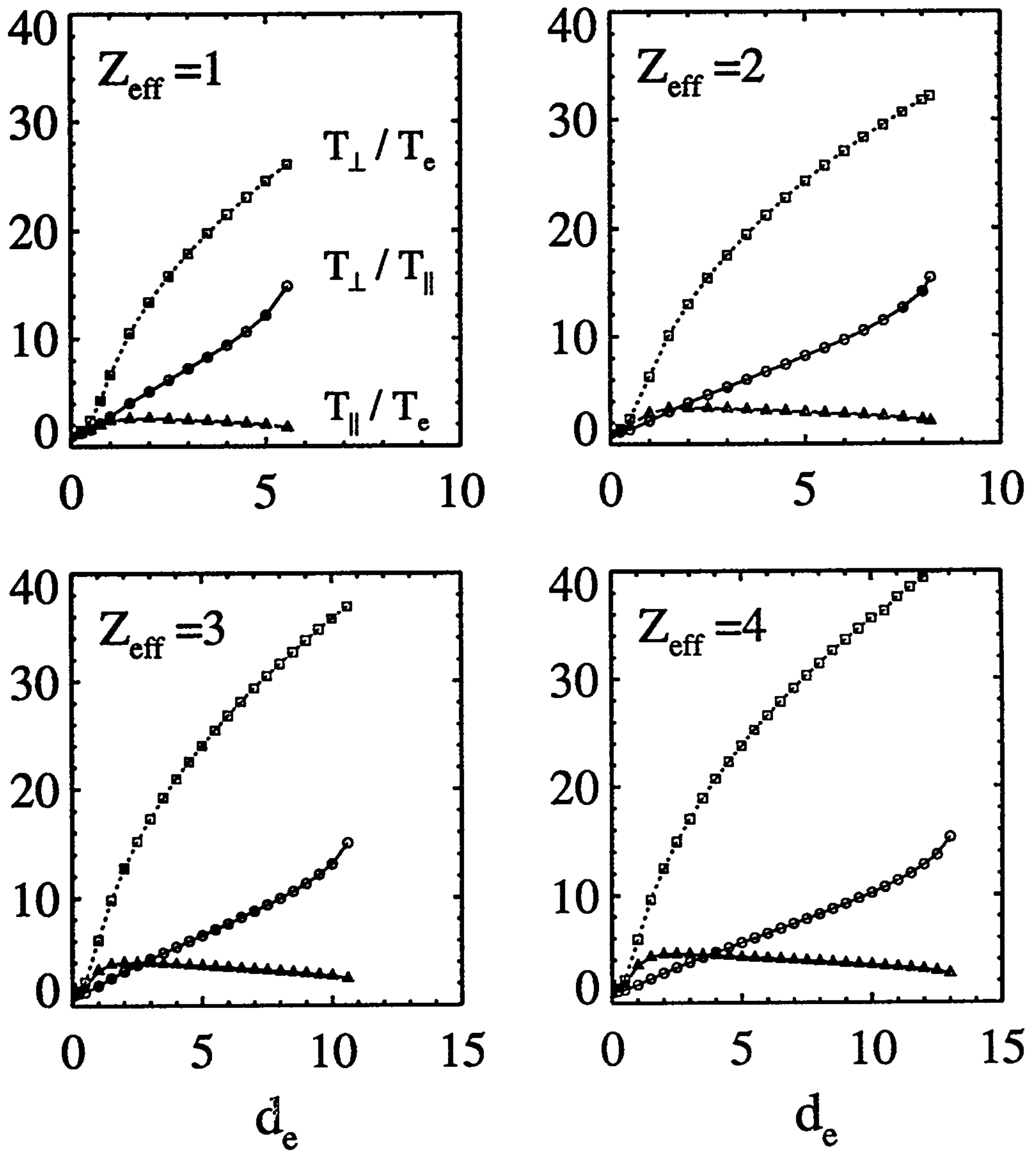

Figure 10: Temperature anisotropy with $Z_{eff} = 1, 2, 3, 4$. $\nu_L/\nu_0 = 0.03$ and $\delta = 5\,\%$.

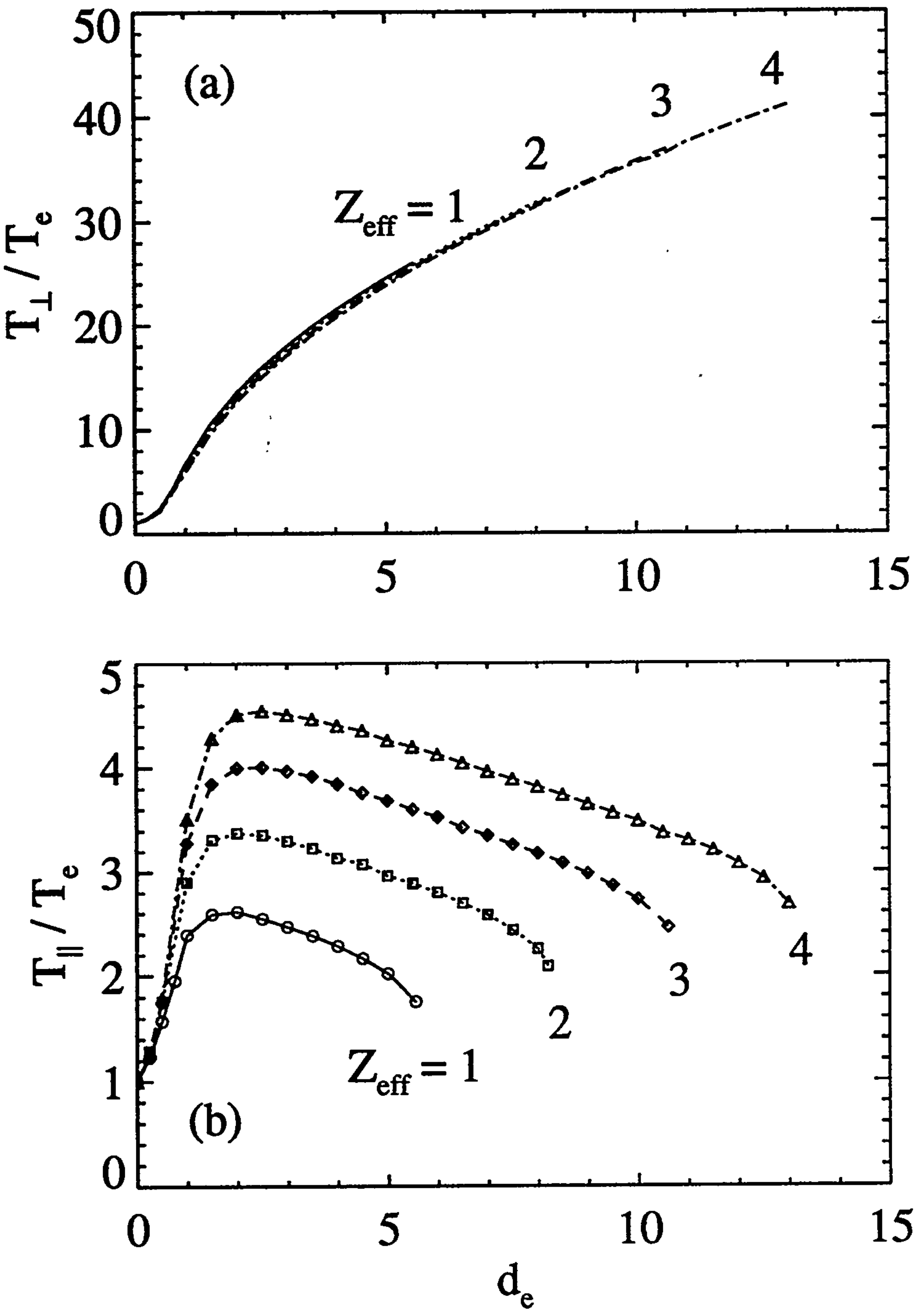

Figure 11: Z_{eff} dependence of perpendicular and parallel temperature. With a larger Z_{eff}, $T_{\|}$ is larger and $T_{\perp}$ is smaller due to more frequent pitch angle scattering. $\delta = 5\,\%$ and $\nu_L/\nu_0 = 0.03$.

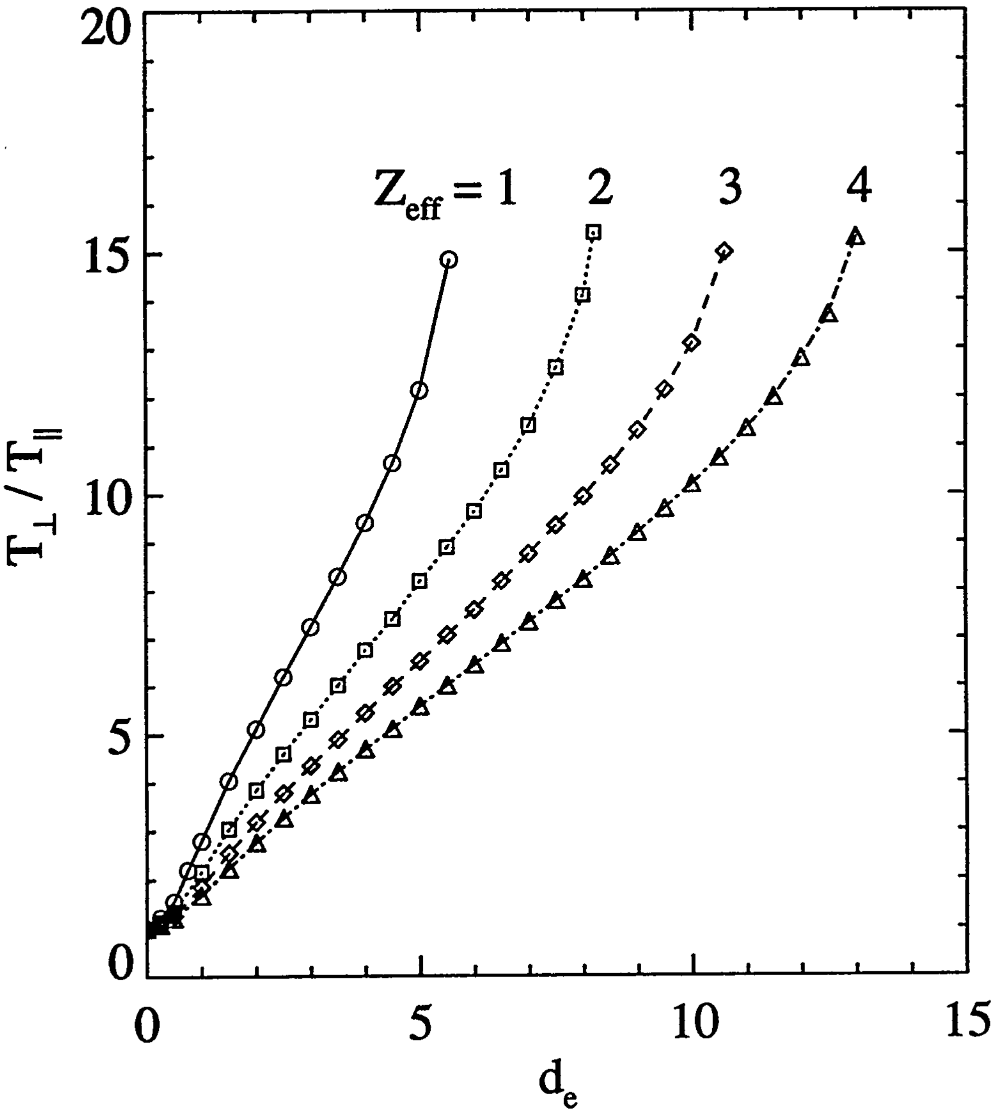

Figure 12: Warm electron temperature anisotropy with various values of Z_{eff}. $\delta = 5\,\%$ and $\nu_L/\nu_0 = 0.03$.

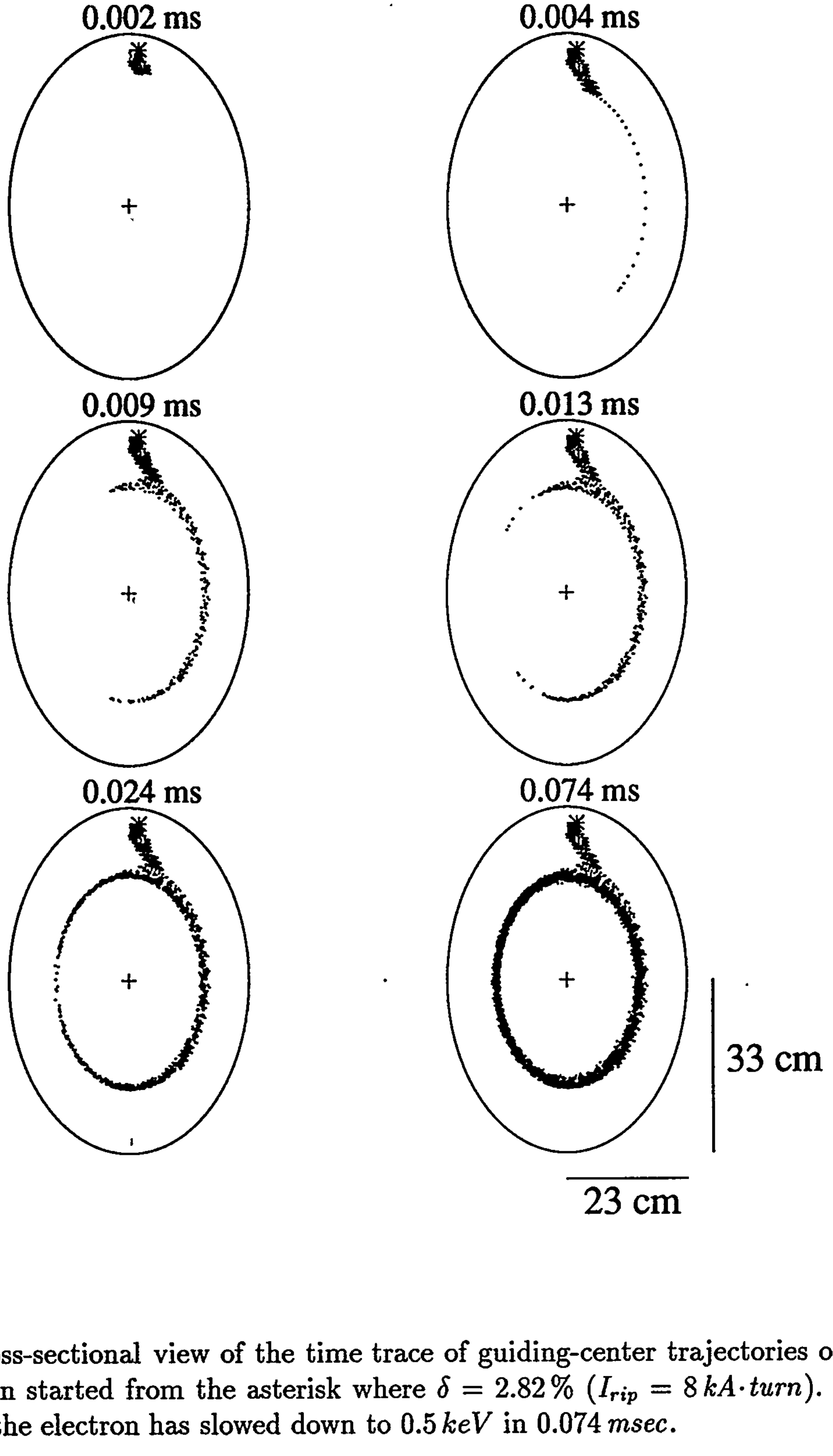

Figure 13: Cross-sectional view of the time trace of guiding-center trajectories of a $1.5\,keV$ electron started from the asterisk where $\delta = 2.82\,\%$ ($I_{rip} = 8\,kA\cdot turn$). In the final plot, the electron has slowed down to $0.5\,keV$ in $0.074\,msec$.

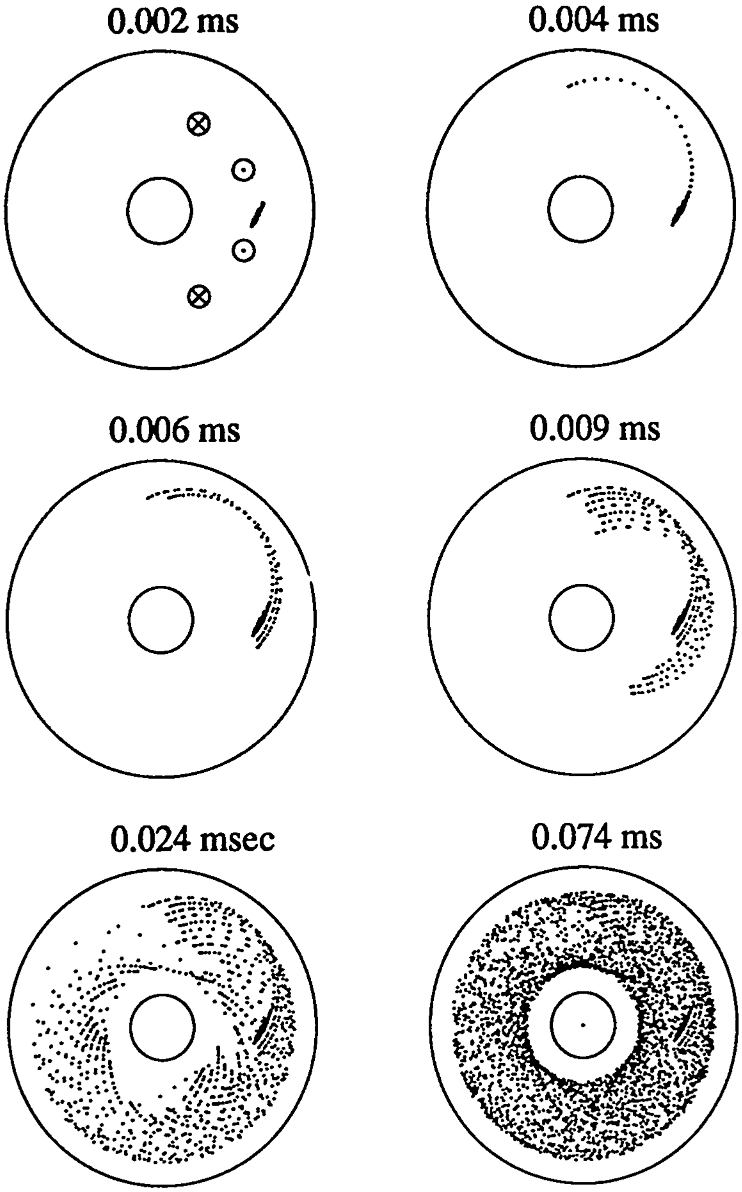

Figure 14: Time trace of test electron orbits in the presence of ripple fields. View from the top of the machine. The location of ripple coils are seen in the first plot with directions of current flowing ($W_0 = 1.5\,keV, I_{rip} = 8\,kA\cdot turn$).

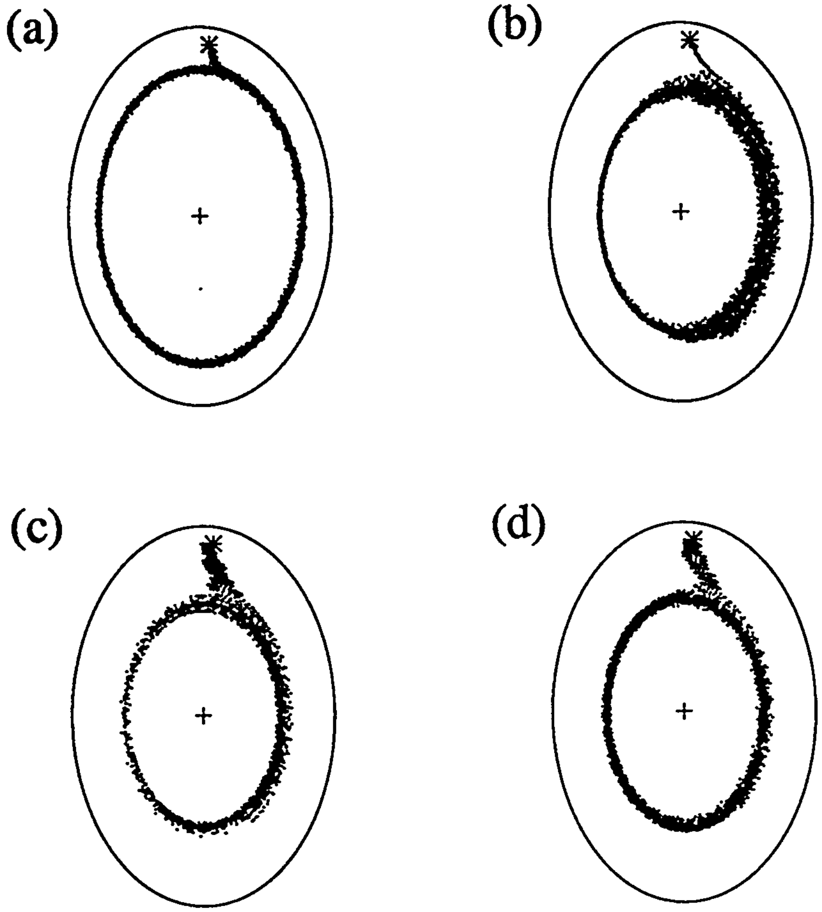

Figure 15: The radial penetration depth can be controlled by changing the ripple strength and the electron energy. (a) $I_{rip} = 4\,kA{\cdot}turn$ (1.45 % at the starting point) and $W_0 = 0.7\,keV$, (b) $I_{rip} = 4\,kA{\cdot}turn$ (1.45 %) and $W_0 = 2.0\,keV$, (c) $I_{rip} = 10\,kA{\cdot}turn$ (3.50 %) and $W_0 = 0.7\,keV$, (d) $I_{rip} = 8\,kA{\cdot}turn$ (2.82 %) and $W_0 = 1.0\,keV$. Either higher particle energy or larger ripple strength is necessary to get a sufficient penetration.

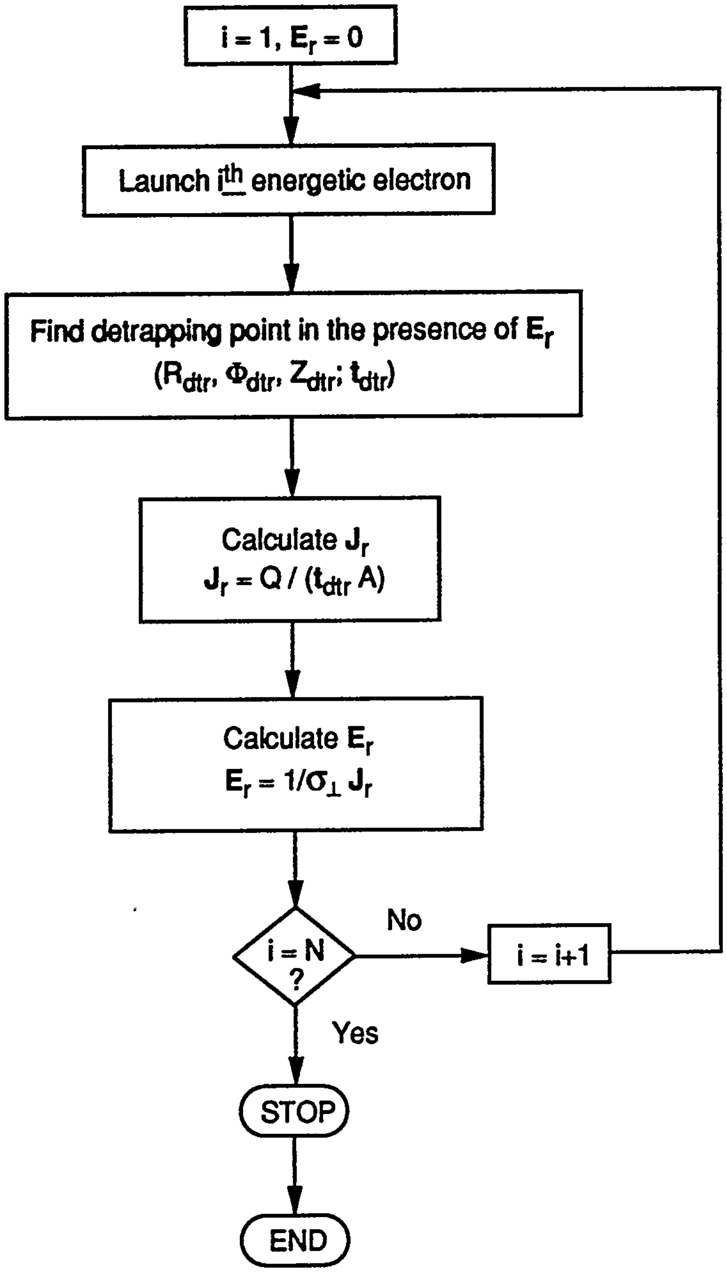

Figure 16: Algorithm for calculating radial electric fields generated by ripple-injected electrons.

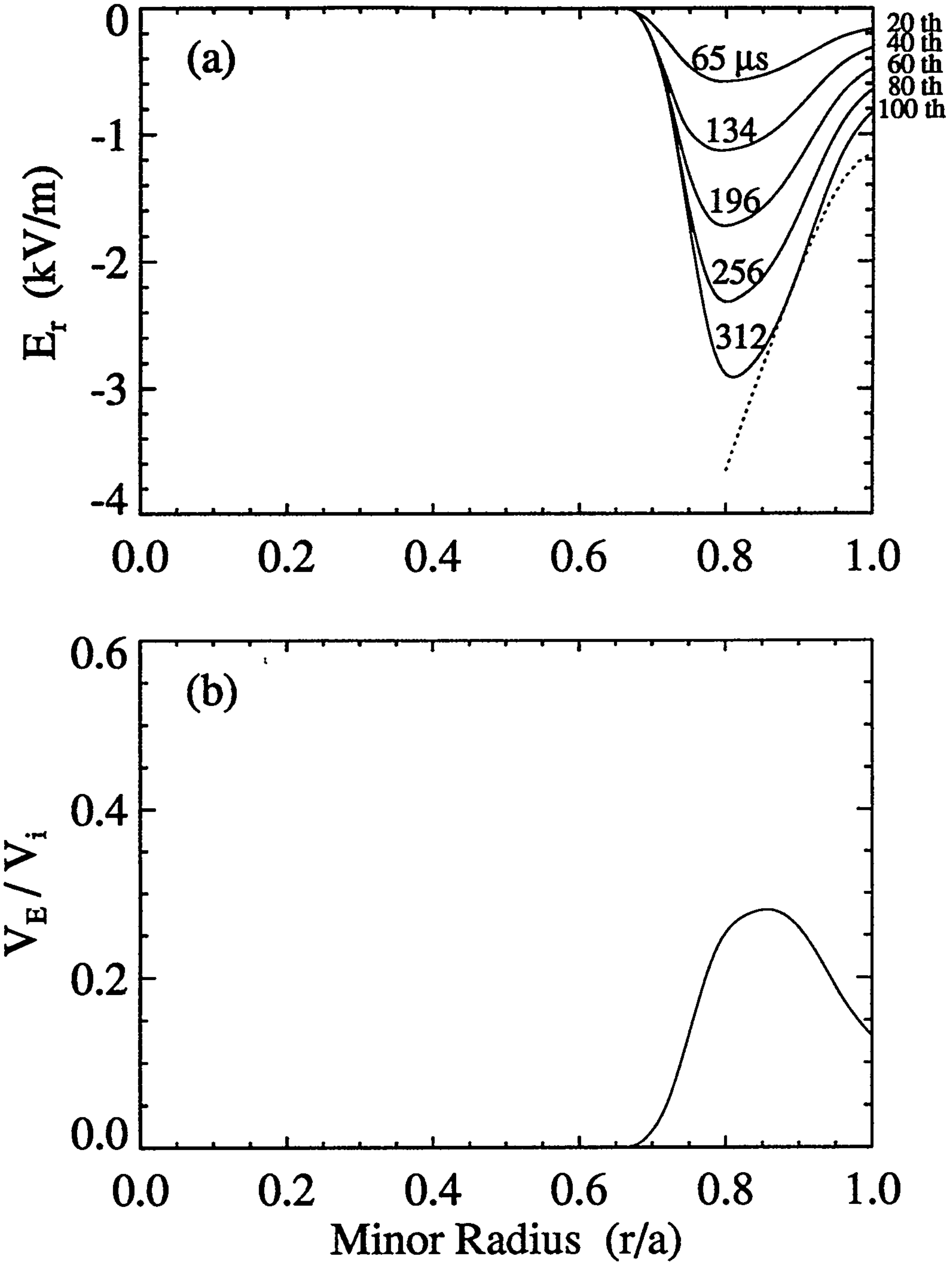

Figure 17: (a) Time trace of radial profiles of electric fields. Dotted curve indicates the required electric field above which a bifurcation occurs. (b) $\mathbf{E} \times \mathbf{B}$ rotation speed normalized by ion thermal speed generated by sequential deposition of 100 energetic electrons. The deposited charge per electron is assumed to be $Q = -4.6 \times 10^{12}\, e$ and $W_0 = 1.0\, keV$ and $I_{rip} = 8\, kA\cdot turn$.

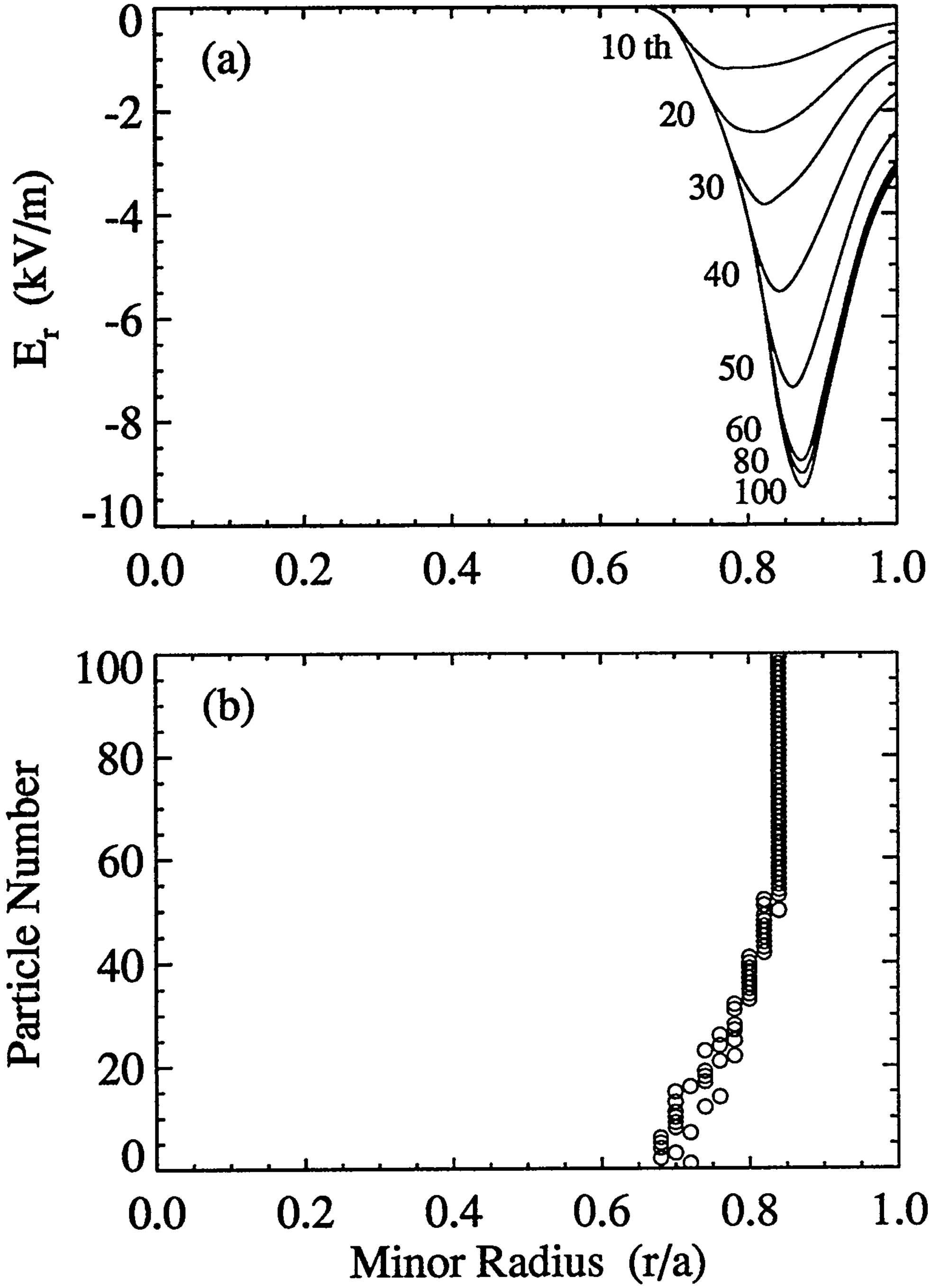

Figure 18: (a) Electric field profiles generated by 10, 20, 30, 40, 50, 60, 80, and 100 electrons, and (b) the radial locations of 100 launched electrons where detrapping occurs. $Q = -1.8 \times 10^{13}\, e$ and $W_0 = 1.0\, keV$ and $I_{rip} = 8\, kA \cdot turn$.

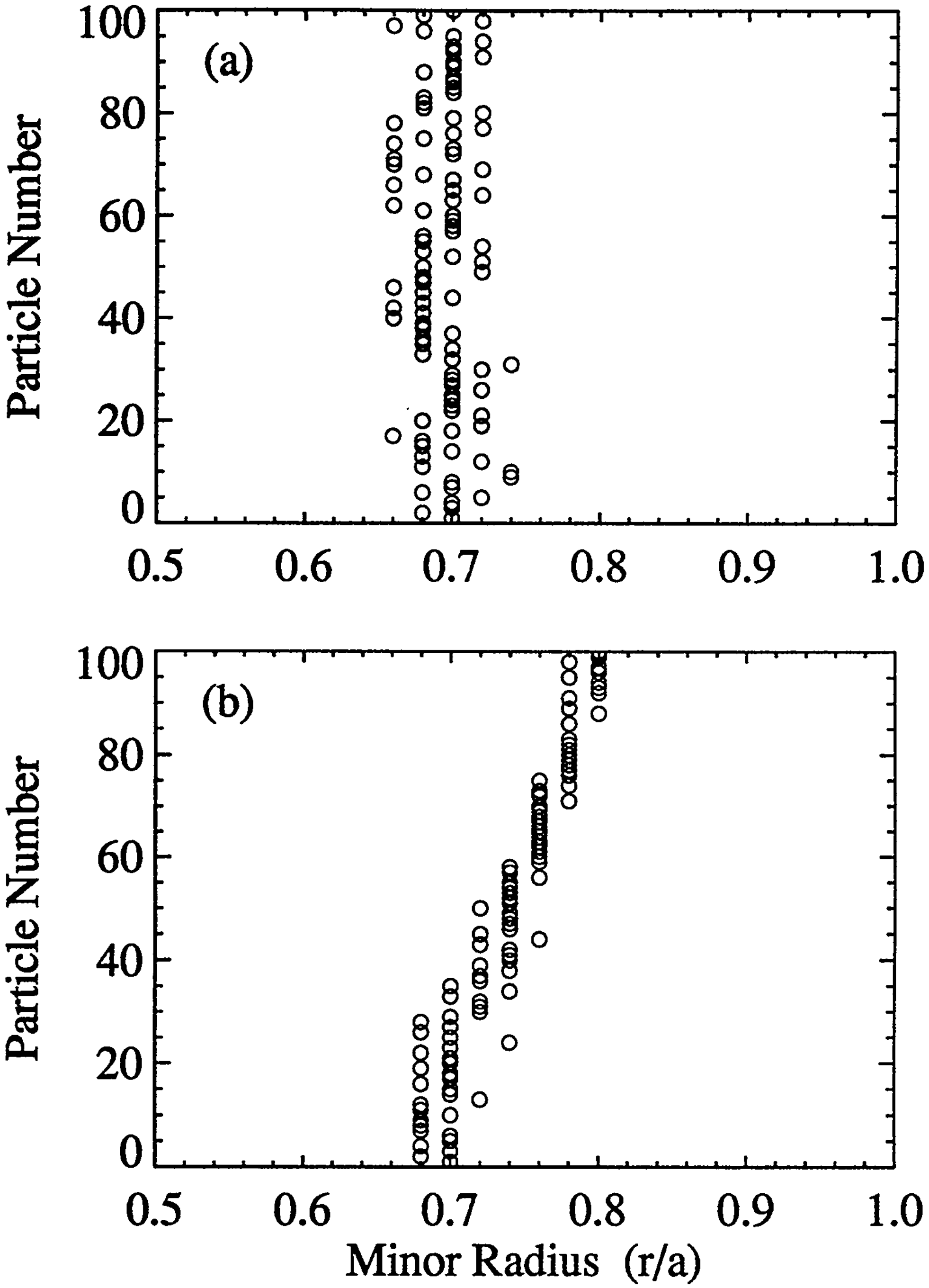

Figure 19: Plot of detrapping points of 100 sequentially launched electrons. Initial electron energy is $W_0 = 1.0\,keV$ and $I_{rip} = 8\,kA\cdot turn$ (2.82%). (a) Radial electric fields are not considered in the calculation of electron orbits ($Q = 0$), (b) radial electric fields are included ($Q = -6.0 \times 10^{12}\,e$). In this case, electrons cannot penetrate as much as the case without electric fields since $\mathbf{E}\times\mathbf{B}$ drifts hinder the radial penetration.

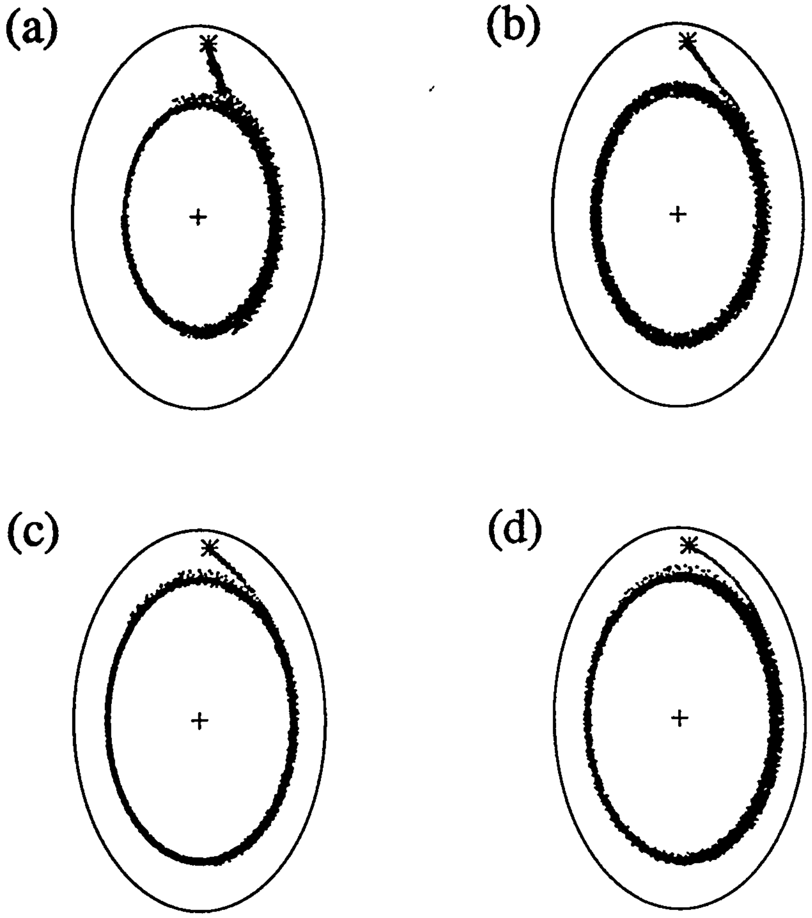

Figure 20: Orbits of the (a) 1^{st}, (b) 22^{nd}, (c) 48^{th}, and (d) 100^{th} electron among 100 launched electrons. $I_{rip} = 8\,kA{\cdot}turn$, $Q = -1.2 \times 10^{13}\,e$, $W_0 = 1.0\,keV$. Electrons become less penetrative as E_r build up.

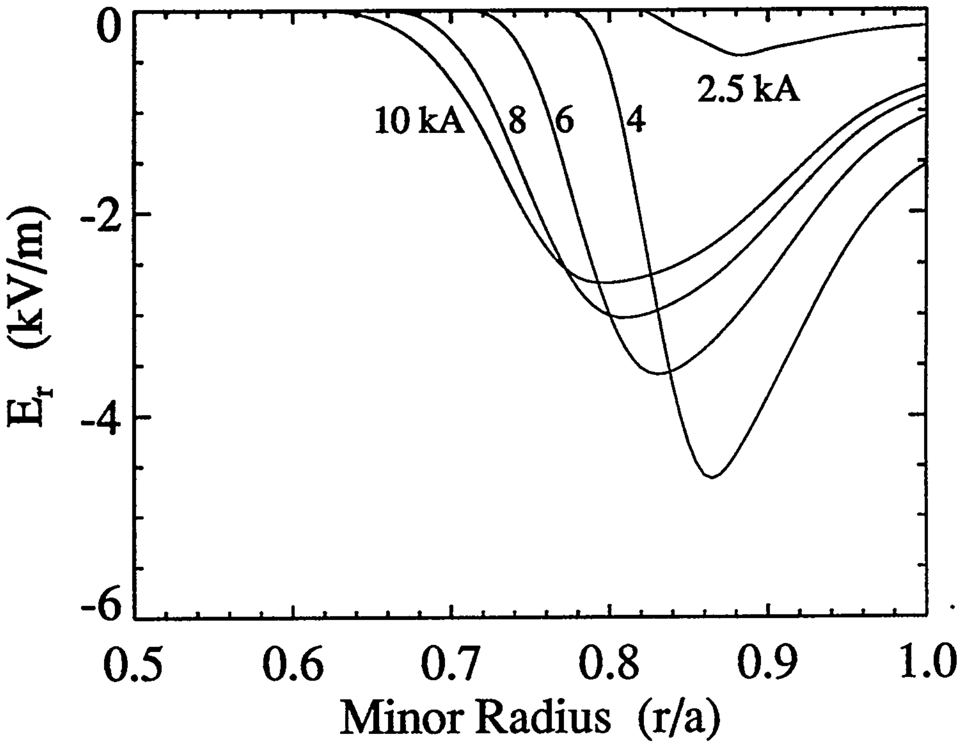

Figure 21: The electric field profiles with several different ripple strengths. The strength of ripple at the starting position corresponds to 0.92 % (2.5 *kA·turn*), 1.45 % (4 *kA·turn*), 2.15 % (6 *kA·turn*), 2.82 % (8 *kA·turn*), and 3.50 % (10 *kA·turn*), respectively. Energetic electrons are launched with initial energy $W_0 = 1.0\,keV$ and $Q = -4.6 \times 10^{12}\,e$.

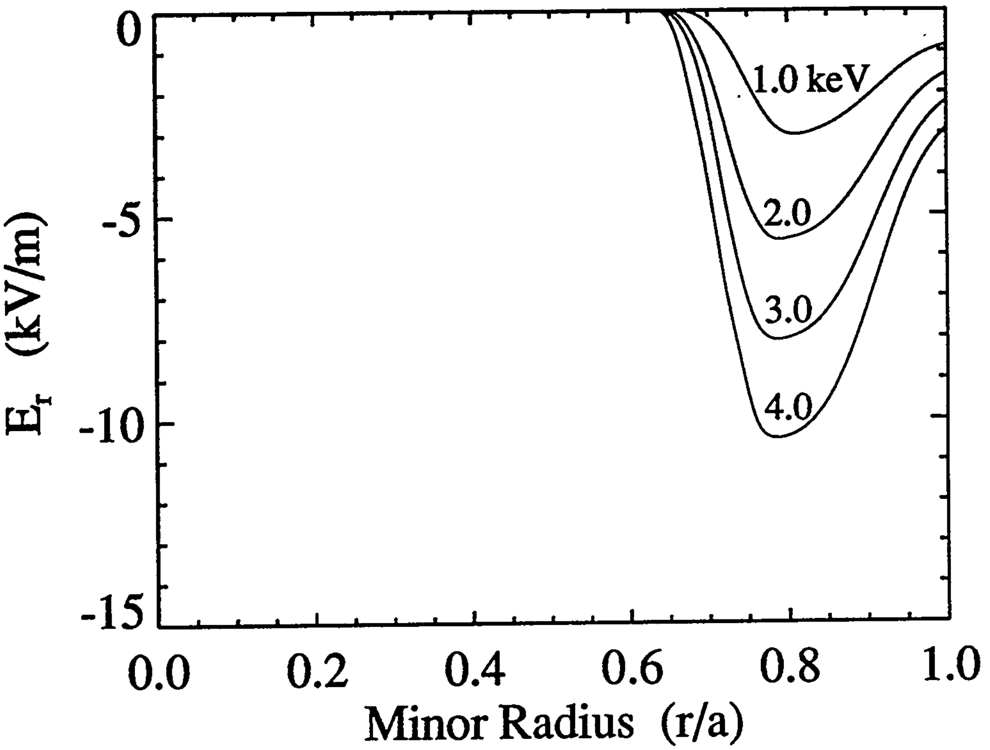

Figure 22: The electric field profiles with several different initial energy. $Q = -4.6 \times 10^{12}\,e$ and $I_{rip} = 8\,kA \cdot turn$.

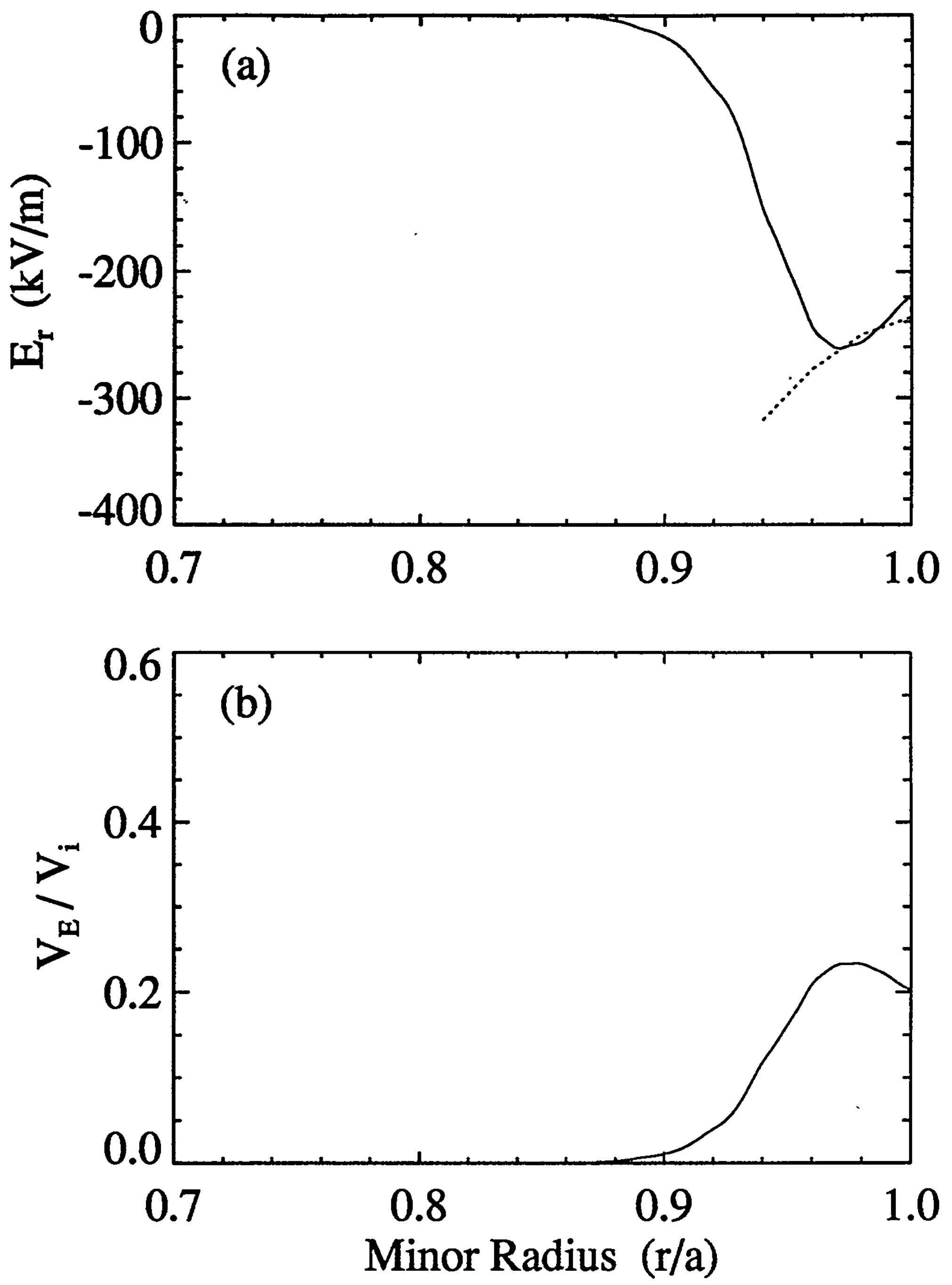

Figure 23: Similar run with ITER parameters. (a) Electric field profile, and (b) $\mathbf{E}\times\mathbf{B}$ rotation speed normalized by ion thermal speed. $Q = -2.0 \times 10^{15}\, e$, $W_0 = 80\, keV$, and $I_{rip} = 0.8\, MA \cdot turn$.